uc3m | Universidad Carlos III de Madrid

University Degree in Aerospace Engineering

2018-2019

Bachelor Thesis

"Experimental Analysis of Hydrogen Premixed Flame Instabilities"

Bartłomiej Kokot

Advisor: Mario Sánchez Sanz

Leganés, July 2019

ABSTRACT

An analysis of the results of a hydrogen-air combustion experiment is carried out in this project.

The main objective of this experiment is to study the instabilities of hydrogen-air premixed laminar flames propagating in a confined combustion chamber. The combustion chamber has a rectangular prismatic shape of $950 \times 200 \times (1 - 10)$ mm (height $\times$ width $\times$ thickness). The flames travel vertically from the top of the chamber, which is open to the ambient, to its closed bottom. There are two parameters that are varied to study their effect: mixture equivalence ratio (from 0.27 to 2.0) and combustion chamber thickness (from 1 mm to 10 mm). There are also two raw outputs: high-speed videos (recorded using a Schlieren system) and pressure measurements.

In this project, an ImageJ macro and a Matlab script are developed to semi-automatically analyze the recorded images and obtain flame instantaneous position, propagation speed, and length. These data, along with the pressure measurements, allow to identify the different kinds of flame instabilities (hydrodynamic, thermodiffusive, and thermoacoustic) and to plot a "stability map" (Fig. 6.1) as a function of equivalence ratio and chamber thickness.

Also, a new kind of instability characterized by fractal patterns, is found for very lean mixtures in a very thin chamber. This finding is not described in the literature. It is hypothesized that this phenomenon is due to large heat losses when the chambers walls are close to each other.

Keywords: Flame instability, premixed hydrogen-air, experiments, image processing

RESUMEN

El objeto del presente proyecto es el análisis de los resultados de un experimento de combustión premezclada de hidrógeno.

El principal objetivo de dicho experimento es estudiar las inestabilidades de las llamas premezcladas de hidrógeno con aire en una cámara de combustión. La cámara tiene forma de prisma rectangular de dimensiones $950\times200\times(1-10)$ mm (alto $\times$ancho $\times$ espesor). Las llamas viajan verticalmente desde la parte superior, que está abierta al ambiente, hasta la parte inferior, que está cerrada. Hay dos parámetos que se varían para evaluar su efecto: el dosado (desde 0.27 hasta 2.0) y el espesor de la cámara de combustión (desde 1 mm hasta 10 mm). También se obtienen dos tipos de resultados brutos: vídeos de alta velocidad (grabados usando la técnica Schlieren) y mediciones de presión dentro de la cámara.

En este proyecto se desarrolla una macro de ImageJ y un programa de Matlab que permiten analizar de forma semiautomática las grabaciones y obtener datos relevante como posición del frente de llama, su rapidez de propagación y longitud. Esos datos se usan junto con las mediciones de presión para identificar los distintos tipos de inestabilidades de llama (hidrodinámica, termodifusiva, termoacústica) y dibujar un "mapa de estabilidad" (Fig. 6.1), en función del dosado y del espesor de la cámara.

Además, se identifica un nuevo tipo de inestabilidad caracterizado por frentes de llama cortos que se propagan siguiendo patrones fractales. Este fenómeno tiene lugar en mezclas extremadamente pobres, cuando el espesor de la cámara es de 4 mm o menor, y no está descrito en la bibliografía. Se plantea la hipótesis de que se debe a las mayores pérdidas de calor cuando se reduce la distancia entre las paredes de la cámara combustión.

Keywords: Inestabilidad de llama, premezcla hidrógeno-aire, experiemento, procesamiento de imágenes

ACKNOWLEDGEMENTS

The author wants to thank the advice and support of Fernando Veiga-López in the analysis of experimental data.

CONTENTS

LIST OF FIGURES

LIST OF TABLES

1. INTRODUCTION

An analysis of the results of a hydrogen-air combustion experiment is carried out in this project. This experiment was recently performed by Veiga-López, Daniel Martínez-Ruiz, Mike Kuznetsov, and Mario Sánchez-Sanz [1] at the Karlsruhe Institute of Technology, in collaboration with the Thermal and Fluids Engineering Department at Universidad Carlos III de Madrid. Some of the results are presented and analyzed in [1]. Others have not been yet published.

This project is intended to provide a basic analysis of all the results of their experiment. Such an analysis is a preliminary stage before studying more advanced parameters and features, such as the Markstein and Lewis numbers.

The layout of this paper is as follows. After a review on basic flame instabilities in Chapter 2, the objectives of the project are presented, along with a bibliographic review supporting the proposed solution, in Chapter 3. A detailed description of the experiment and the project methodology are presented in Chapter 4. Even though image post-processing and analysis is actually a part of the methodology, Chapter 5 is exclusively dedicated to this subject, since it is an extensive and crucial part of the project. The results are presented and discussed in Chapter 6, and conclusions and possible future research are in Chapter 7.

Finally, Chapter 8 is dedicated to project management aspects, i.e., regulatory and socioeconomic frameworks, including real-life applications, and project time planning and budget.

2. PRINCIPLES OF FLAME INSTABILITIES

This chapter is intended to give an overview on the different types of premixed flames instabilities, their causes and effects, as well as formal definitions of the variables used in this paper.

2.1. Classification

Steady planar premixed deflagration rarely exists. Instabilities of premixed flame fronts can be classified in three families [2]:

- Hydrodynamic instabilities. The most notable instability of this kind is the Darrieus-Landau (DL) instability. It was independently predicted by G. Darrieus and L. Landau in the 1940's. They both used an incompressible flow model, in which an infinitesimally thin reaction front propagates perpendicular to itself at a constant speed [3]. The density change across the flame due to thermal expansion of the gas results in a curved flame front, with cells much larger than the flame thickness [2].

  Another type of hydrodynamic instability is the Rayleigh-Taylor (RT) instability. It is due to buoyant convection when the flame propagates against the gravity, i.e., from the bottom to the top [4].

- Thermo-diffusive instabilities. They result from competition between molecular diffusion and thermal diffusion through the flame thickness. In gaseous combustion, it takes the form of "cellular", or wrinkled, flames. Small cells, of the order of the flame thickness, appear on the front, usually superimposed to DL, and have a chaotic aspect.

  Cellular flames are observed in rich mixtures of heavy hydrocarbon fuels and in lean mixtures of light fuels, such as hydrogen or methane. This phenomenon occurs when the Lewis number (molecular diffusion coefficient of the limiting species to thermal diffusion coefficient of the mixture ratio) is smaller than 1. [2, 5].

- Thermo-acoustic instabilities. They appear because of the two-way coupling between combustion exothermicity and pressure waves present in the combustion chamber [1, 6]. As a consequence, the flame front oscillates around its mean propagation speed in sync with the acoustic field.

  Two different regimes can be identified among thermoacoustic instabilities:

  - Primary (or acoustic) instabilities. The associated acoustic pressure is around $\Delta p \approx 500$ Pa. In experiments involving premixed combustion in tubes, they always rapidly develop around the midpoint of the tube, regardless its total

length, and from that point on, the pulsating flame travels down to the bottom of the tube.

– Secondary (or parametric) instabilities. In some cases, a primary instability can evolve into a violent secondary instability. The acoustic pressure reaches a maximum of about 5 kPa, and then decreases slowly [2]. The secondary instabilities may stabilize the DL instability, resulting in a planar flame with large pulsating cells [1].

2.2. Coupling and Damping Mechanisms

Thermoacoustic instabilities are due to different coupling mechanisms, that compete with damping mechanisms. Essentially, coupling occurs when a variable of the flow (pressure, speed or acceleration) modulates the heat release rate of the reactive front. This affects the thermal expansion of the gas, which in turn has an influence on the flow. Depending on the phase and gain of the feedback, this loop may lead to amplification (destabilizing effect) or attenuation of the waves (stabilizing effect) [1, 2]. There are three main coupling mechanisms [2]:

- Pressure coupling. It is the simplest mechanism. Adiabatic compression due to the acoustic waves changes the temperature of the gas, which in turn changes the heat release rate.
- Velocity coupling. It is the dominating mechanism in the Rijke tube, in which the heat transfer from the gauze to the air is directly proportional to the flow velocity.
- Acceleration coupling. It seems to be responsible for primary instability of flames in tubes. The periodic acceleration of the flow may change the surface area of the flame front, hence changing the global heat release rate.

On the other hand, damping mechanisms include viscous dissipation, heat transfer through the boundary layer at the walls, acoustic radiation through exhaust orifices, phase lags, inhomogeneities of the unperturbed flow, etc [2]. The most important among these are heat losses by conduction and acoustic viscous dissipation. Both are closely related to the combustion chamber thickness h.

The relative importance of heat losses through chamber walls can be estimated by comparing the conductive heat flux, q_k, with the flame heat release rate, q_f:

$$\Delta = \frac{q_k}{q_f} \sim \frac{W\delta_T k_g (T_b - T_u)/h}{Wh\rho S_L c_p (T_b - T_u)} = \frac{\delta_T k_g}{h^2 \rho c_p S_L} = \left(\frac{\delta_T}{h}\right)^2, \tag{2.1}$$

where W is the combustion chamber width, δ_t is the thermal flame thickness, k_g is the air thermal conductivity, T_b is the temperature of combustion products, T_u is the ambient

temperature, h is the chamber thickness, ρ is the unburnt mixture density, S_L is the laminar flame velocity, and c_p is the air specific heat. Recall that $D_T = k_g/(\rho c_p)$ is the thermal diffusivity coefficient and that $\delta_T = D_T/S_L$.

In other words, heat losses through walls conduction are larger for thinner chambers and leaner mixtures (thicker flame front). When the heat losses are of the order of flame heat release, i.e., when $\Delta \sim O(1)$, flame extiction is expected.

On the other hand, acoustic losses can be estimated by comparing the residence time of a sound wave, t_a, and the acoustic dissipation time, t_d:

$$\frac{t_a}{t_d} \sim \frac{2L/c}{\rho h^2/\mu} = \frac{2\nu L}{ch^2}, \tag{2.2}$$

where L is the height of the combustion chamber, c is the sound speed at a characteristic temperature $T \sim (T_b + T_u)/2$, and μ and ν are the dynamic and kinematic viscosities respectively. A low value of the t_a/t_d ratio means that the attenuation of pressure waves takes a relatively long time, so acoustic energy losses by viscous dissipation are small.

Finally, the relative importance of losses by radiation of acoustic energy through the open end of the chamber can be estimated in a similar way:

$$\frac{t_a}{t_{rad}} \sim \frac{2L/c}{cL/(\omega h)^2} = \frac{2(\omega h)^2}{c^2}, \tag{2.3}$$

where ω is the angular frequency of the acoustic wave. However, note that this ratio t_a/t_{rad} is always very small due to the c^2 in the denominator.

So, it can be concluded that heat and acoustic energy losses are strongly dependent on the geometry of the combustion chamber, particularly on the chamber thickness h.

A detailed order-of-magnitude analysis can be found in [7].

2.3. Flame Position and Speed Definitions

In this section, the definitions of flame position and speed used in this paper are provided. The nomenclature and definitions themselves are based on those used in [7, 8]. Refer to Fig. 4.1 for the meaning of the system of coordinates and geometric variables used here.

Burnt volume, V_b, refers the volume of combustion products. Since the chamber thickness is small compared to chamber height and width, it is useful to define a *burnt area*, $A_b = V_b/h$, where h is the chamber thickness. The burnt area can be measured on the images taken in the experiment (see Section 4.1), by assuming that the position of the flame front is constant along z axis. The latter is normally a good approximation on the global combustion chamber scale.

Mean flame front position, x_f is defined here as the *instantaneous* distance from the

upper end of the chamber to the flame front, *spatially* averaged over the y (horizontal) coordinate. So, formally, $x_f = A_b/W$, where W is the chamber width.

Similarly, *mean flame speed*, U_L, is the *instantaneous* flame propagation speed, *spatially* averaged over the y (horizontal) coordinate. In other words, it is the derivative of that mean position in time: $U_L = \mathrm{d}x_f/\mathrm{d}t$.

The average in time of this mean speed is termed in this paper *average speed*, $U_{avg} = L/t_b$, where L is the chamber height and t_b is the total combustion time.

Another possible definition of flame position is the distance of a single representative point (e.g. the middle one) to the chamber end. For instance, it used in [9]. However, it may lead to misleading results in the case of secondary thermoacoustic instabilities, where the "funnels" penetrating in the burnt gas oscillate at a frequency half the acoustic frequency [1].

3. PROBLEM STATEMENT

In this chapter, the motivation and objectives of the project are presented, based on a bibliographic review.

3.1. Historical Background

The so-called "singing flame" was the first thermoacoustic phenomenon to be observed and investigated. In 1777, Byron Higgins obtained clear musical tones by placing the nozzle of a hydrogen burner inside a vertical tube open at both ends. In 1802, the German physicist Ernst Chladni showed that the flame excites the fundamental mode of the tube or one of its harmonics. On the other hand, the "dancing flame" was first reported by John Le Conte in 1858. During a musical party, he observed that the flame of a gas burner oscillated in sync with the music [10]. Thermoacoustic instabilities in tubes were also studied by Ernest-François Mallard and Henri Louis Le Chatelier, as part of their research on combustion applied to mining safety.

Around 1850, Pieter Rijke discovered that sound can be also generated in a tube by means of other heat sources, such as a heated metal gauze, placed at a specific location in the tube [6, 11]. In 1878, Lord Rayleigh formulated a general criterion explaining acoustic waves amplification by heat addition [12]. This criterion has been restated and verified over the years, and its validity can be proven analytically [6].

In the early 1940's, Georges Jean Marie Darrieus (also known for inventing the vertical axis wind turbine) and Lev Landau independently predicted the existence of hydrodynamic instabilities, which are often referred to as Darrieus-Landau (DL) instabilities [2].

In the following decades, first thermoacoustic theories started to be developed. In 1953, Kaskan proposed that thermoacoustic coupling is due to flame surface area variations within the boundary layer near the walls of the tube. Short after that, however, Markstein and Leyer produced experimental and theoretical evidence suggesting that coupling is a result of flame surface variation due to the onset of a cellular structure [13].

3.2. Bibliographic Review

Until not long ago, flame instabilities were just a laboratory curiosity. However, as rocket engines and large burners for industrial applications started to be developed, unstable combustion became a concern and an important subject of research [14]. For a detailed list of real-life importance of flame instabilities, see Section 8.1.

Flame instabilities are rarely observed in diffusion flames [14], for this reason current

studies focus on premixed combustion. Hydrocarbons (mainly propane and methane) are mostly used in experiments, since they are cheap and easy to handle. Gaseous hydrogen, however, is emerging as an alternative, offering the advantage of much broader flammability limits.

Most previous experimental studies focused on premixed hydrocarbon flames in tubes, propagating toward the closed end of the chamber [13, 15]. Other combustion chamber geometries found in the literature are Taylor-Couette burner [16], and Hele-Shaw cells [7], always using premixed hydrocarbons. All these authors reported oscillatory behavior of the flame, finding that rich flames are more stable than lean flames. Only in [7] results sensitivity on geometric parameters is meticulously assessed.

Al-Sarraf et al. [17], and Almarcha et al. [18] studied flame instabilities in vertical Hele-Shaw cells with acoustic dampers at the bottom. They did not report any acoustic phenomena, just hydrodynamic and thermodiffusive ones.

A relatively little amount of experiments with premixed hydrogen have been carried out. In particular, Yañez et al. [9] studied premixed hydrogen flames propagating downward in a square tube. They found both primary and secondary thermoacoustic instabilities only for very lean mixtures. Recently, Veiga-López et al. [1] performed a similar experiment using a vertical Hele-Shaw cell, and assessing the effect of the cell thickness.

Mathematical models describing unstable flame behavior are extremely complex, and are applicable only to simple cases. The recent book by Clavin and Searby [2] is a good compendium of current knowledge on analytical unstable flames analysis. It is also noteworthy that the importance of the Markstein number effect on thermoacoutics was introduced by [16], and confirmed by [7]. Recently, Yoon et al. [15] found a correlation between the prduct βM, being β and M the Zeldovich and the Mach numbers respectively, and the average acoustic pressure.

A few numerical studies have been also performed, using simplified models. Petchenko et al. [19] numerically reported both primary and secondary thermoacoustic regimes in a flame toward the closed end of a narrow channel. Later, in another paper [20], these authors included the effect of the channel thickness and found that oscillations are stronger in thicker channels. On the other hand, Fernández-Galisteo et al. [4] used the low-Mach number approximation and found instabilities that wrinkled the flame but could not reproduce acoustic effects due to the incompressibility assumption.

Given the complexity of the mathematical models of flame instabilities, experimental analysis is the most reliable way of studying them. On top of that, no experiments involving premixed hydrogen combustion in a Hele-Shaw cell are found in the literature. A Hele-Shaw cell has the advantage of easily adjustable geometry.

This project is intended to contribute to the work done by Veiga-López et al. [1], and perform a basic analysis of all the results of their experiment. Such an analysis is a preliminary stage before studying more advanced parameters and features, such as the

Markstein and Lewis numbers.

3.3. Objectives

The ultimate goal of this project is to give a qualitative and quantitative description of the different phenomena that occur during hydrogen-air mixture deflagration in a thin combustion chamber, as well as the transition between them, on an experimental basis.

In particular, two effects are considered: the equivalence ratio, to study the effect of the composition of the mixture, and the combustion chamber thickness, to assess the effect of viscous dissipation and heat losses by conduction. On the other hand, two outputs are analyzed: high-speed videos recorded using Schlieren imaging, and pressure inside the chamber measurements.

For that purpose, specialized software has to be developed, to allow semi-automatic processing of the experimental data.

Among the observed phenomena, thermoacoustic instabilities are the main focus, since they are not yet completely understood and have some importance in industrial applications. For this reason they are currently an important object of research [1, 2, 6].

4. METHODOLOGY

4.1. Experimental Setup and Procedure

The data and images analyzed in this project come from the experiment performed by Veiga-López et al. and presented in their paper [1]. Although the experiment itself does not belong to this project, it is thoroughly described here to give a better understanding of where the experimental data come from.

The following is an extract from the aforementioned paper [1] describing the experiment:

> "A vertical combustion chamber is conformed by two 10-mm-thick flat plexiglass plates separated by a PVC sealing hollow frame. The total volume enclosed by the cell is $950 \times 200 \times (1 - 10)$ mm^3 ($L \times W \times h$). The gap height (h) can be modified to assess its effect.
>
> Fuel and oxidant are mixed before entering the combustion chamber, controlling the fuel-to-air ratio with two EL-FLOW mass flow controllers. The mixture is fed via an injection port located at the top ignition side of the chamber, keeping this end closed and opening the venting valve. The complete charge of the chamber is checked at the outlet line using a gas analyzer Rosemount^{TM} CT5400. After a minute of exposure, the top end is fully reopened and the mixture ignited simultanously by a spark plug.
>
> A Z-shape Schlieren system is used to capture high-speed images of the flame front. A LED light source, two 280-mm-diamater mirrors, a set of lenses and a high-speed camera (Photron FASTCAM SA 1.1) form the optical system. Due to the limited size of the mirrors, only partial visualization of the flame was possible during each experiment. The chamber can be shifted vertically to change the region of interest, thus capturing the whole channel length in several trials. Additionally, a pressure sensor (PCB M113B12) is located at the bottom of the chamber to measure the inner over-pressure". [1]

The experimental setup is also schematically represented in Fig. 4.1.

Rectangular prismatic combustion chambers with one dimension much smaller than the other are frequently referred to as Hele-Shaw cells. The flow inside can be assumed quasi-2D, which simplifies the analysis. Besides, the chamber thickness can be easily modified to study the effect of the chamber geometry. This is more difficult in tubes.

Schlieren imaging is used to visualize and record the flames, because visible emissions from hydrogen flames are very weak, and vary with mixture equivalence ratio [21]. Resulting images show density gradients, so the flame front can be easily identified on them. Fig. 5.1 shows two sample images.

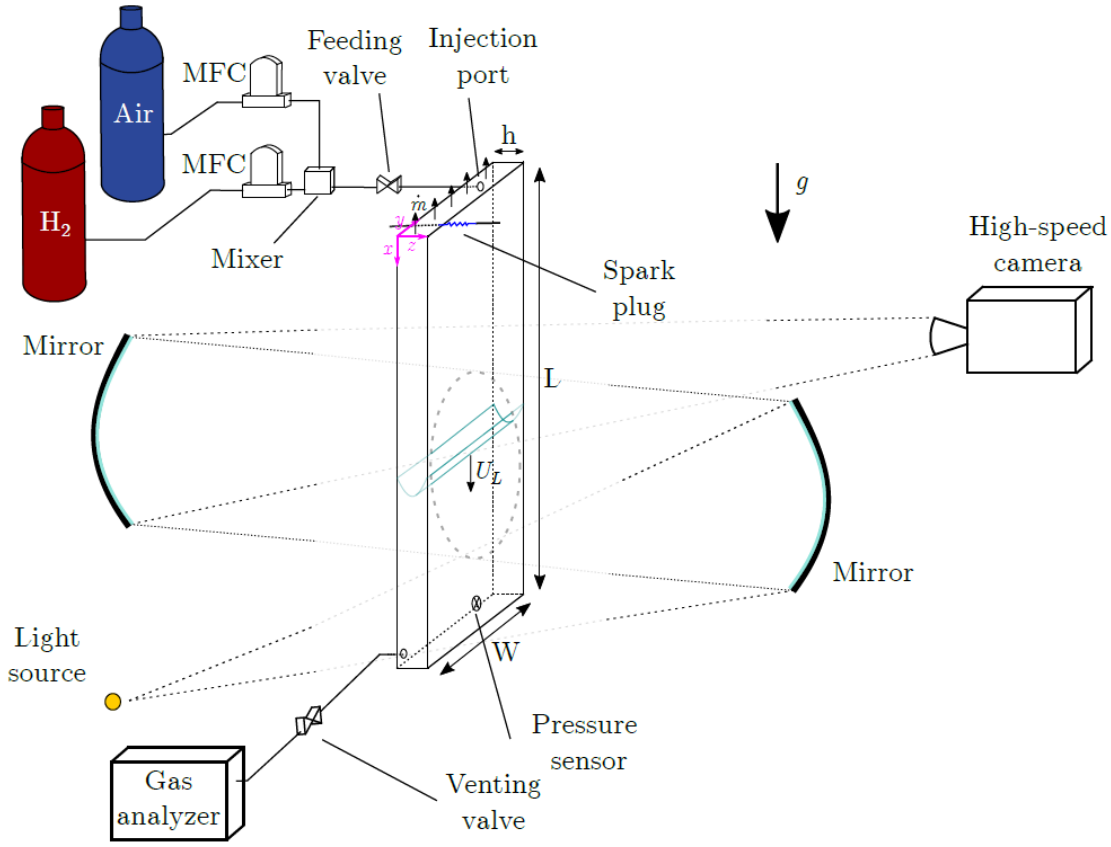

Fig. 4.1. Experimental Setup. The small black arrows at the top of the combustion chamber indicate the open end. Courtesy of Veiga-López et al. [1].

The main limitation of this experimental setup is the relatively small size of the mirrors, which make the visualization of the entire combustion chamber impossible. In most cases, each experiment is recorded in three trials. The three visualization areas are referred to as top, middle, and bottom. Even though time is always measured starting at the activation of the spark plug, random delays in ignition (and other minor random factors) result in slight time incoherence when comparing the videos of the different trials of a single experiment.

In total, 102 experiments with different thicknesses h and equivalence ratios ϕ were successfully performed. The results of cases with h in the range 4-10 mm, and ϕ in the range 0.32-0.51 along with an analysis are presented in [1]. In this project all the results shall be presented, including rich mixtures (up to $\phi = 2$) and very thin combustion chamber (down to $h = 1$ mm).

Table 4.1 summarizes relevant properties of the different mixtures tested in the experiments. ϕ is the equivalence ratio, %vol. H_2 is the hydrogen volume fraction, T_b is the adiabatic flame temperature, S_L is the planar flame speed, Le is the Lewis number, and $\delta_T = D_T/S_L$ is the thermal flame thickness, with $D_T = 2.0 \times 10^{-5} \mathrm{m^2\,s^{-1}}$. These data are taken from [9] and linearly interpolated as needed.

Table 4.1. PROPERTIES OF THE DIFFERENT HYDROGEN-AIR MIXTURES USED IN THE EXPERIMENTS. SOURCE: [9].

ϕ	**%vol. H_2**	**T_b [K]**	**S_L [m/s]**	**Le**	δ_T **[mm]**
0.27	8.00	938	0.06	0.34	0.328
0.29	8.50	975	0.07	0.34	0.274
0.30	8.75	994	0.08	0.34	0.252
0.31	9.00	1013	0.09	0.34	0.233
0.31	9.25	1034	0.09	0.34	0.215
0.32	9.50	1055	0.10	0.34	0.200
0.34	10.00	1093	0.11	0.34	0.182
0.35	10.25	1112	0.12	0.34	0.167
0.36	10.50	1131	0.13	0.34	0.153
0.36	10.75	1150	0.14	0.34	0.143
0.37	11.00	1169	0.15	0.34	0.133
0.41	12.00	1244	0.19	0.35	0.105
0.44	13.00	1319	0.23	0.35	0.087
0.45	13.25	1338	0.24	0.35	0.082
0.46	13.50	1356	0.26	0.36	0.078
0.47	13.75	1375	0.27	0.36	0.075
0.47	14.00	1393	0.28	0.36	0.071
0.49	14.50	1430	0.32	0.36	0.063
0.51	15.00	1466	0.35	0.36	0.057
0.58	17.00	1602	0.57	0.37	0.035
0.64	19.00	1739	0.79	0.39	0.025
0.68	20.00	1807	0.90	0.40	0.022
0.85	25.00	2120	1.55	0.65	0.013
1.02	30.00	2432	2.20	0.91	0.009
1.19	35.00	2309	2.54	1.44	0.008
1.35	40.00	2186	2.88	1.97	0.007
1.52	45.00	2047	2.74	2.03	0.007
1.69	50.00	1907	2.59	2.08	0.008
1.86	55.00	1763	2.23	2.12	0.009
2.03	60.00	1618	1.86	2.15	0.011

4.2. Methodology

To achieve the objectives, the experimental data obtained by Veiga-López et al. is to be analyzed. A part of their results are presented in [1], some other have not been yet published.

Three main aspects of these experimental data can be studied:

- Flame mean position and propagation speed, as well as their frequency and amplitude (obtained from the video images), to confirm that coupling exists and assess the influence of the different types of instabilities on flame propagation speed.
- Over-pressure inside the chamber, which can be directly used to assess the frequency and energy level of the flame oscillations (if any).
- Qualitative flame front structure (curved, flat, smooth, wrinkled, etc.), which is an important characteristic of the different instabilities.

These aspects are expected to provide objective criteria to distinguish the different phenomena taking place in the combustion chamber.

On the other hand, there are two parameters (which could be also regarded as free variables) that are varied from one experiment to another, to study their effect on the combustion process. These parameters are the combustion chamber thickness, or gap height, h, and the mixture equivalence ratio, ϕ. The latter can be also expressed as volume fraction of hydrogen in the mixture (%vol. H_2).

The specialized software used to perform the analysis in this project are the following:

- ImageJ. It is an open source, Java-based, scientific image processing program. It has been used to post-process the images obtained in the experiments.
- Matlab. It is a powerful numerical-computing environment and programming language developed by MathWorks. It has been used to extract numerical data from the processed images, perform calculations and plot the results.

5. IMAGE ANALYSIS

The Photron camera used in the experiments records videos at 2000 fps, which gives a high data resolution. To automatically analyze such an amount of images, special computational tools are required. Developing such tools is actually quite a challenging task, and it is an important part of this project. This chapter gives an overview on how it is achieved.

5.1. Image Processing

The raw images taken in the experiments are RGB images looking as those in Fig. 5.1. To obtain relevant numerical data, such as flame mean position, speed, etc., the flame front has to be detected on the images. In practice, it means that the image has to be binarized, i.e., processed so that the image shows just a white flame front on a black background.

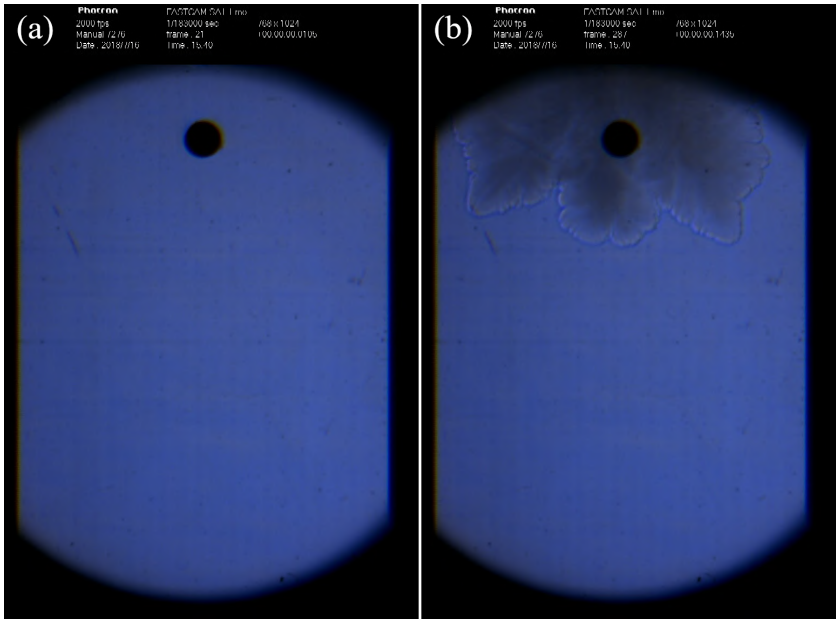

Fig. 5.1. Sample raw images obtained in the experiment with $h = 10\,\text{mm}$ and $\phi = 0.41$, top part of the combustion chamber. The black small circle in the upper part of the visualization is the shadow of one of the screws located on the combustion chamber. Although unintended in principle, these screws have been used as a position reference. (a) First image of the recorded video, with no flame visible. (b) Image taken 0.1435 s after ignition, with the flame front clearly visible.

For that purpose, an ImageJ macro has been developed, which allows to perform a set of operations on a bunch of images. This set of operations giving the desired output has been found by trial and error, and it is as follows:

1. To eliminate pre-existing noise, the image (in this example, Fig. 5.1(a)) is subtracted (using the `Image Calculator` function) to the first image of the experiment (Fig. 5.1(b)), on which no flame is visible. The result is shown in Fig. 5.2(a).

2. The black margins, including the image information at the top, are cropped out.

3. A copy of the resulting image is made, and it is converted into 8-bit grayscale image. See Fig. 5.2(b).

4. In the grayscale image, the noisy background above the flame front is cleaned up using the `Subtract Background` function with a 12-pixel rolling ball. See Fig. 5.2(c).

5. The RGB copy of the image obtained in step 3 is split in its three color channels, and just the red one is kept. See 5.2(d).

6. In this red channel image, the noisy background above the flame front is cleaned up using the `Subtract Background` function with a 12-pixel rolling ball.

7. Both images (i.e., the grayscale image from step 4 and the red channel one from step 6) are summed up together using the `Image Calculator` function. See Fig. 5.2(e).

8. In the resulting image, the noisy background above the flame front is cleaned up using again the `Subtract Background` function with a 12-pixel rolling ball.

9. The image is binarized, with the threshold at 4. In other words, pixels with value larger than or equal to 4 are made white, while all the other pixels are made black. See Fig. 5.2(f).

10. White pixels groups smaller than 10 pixels (which are basically noise) are eliminated, using the `Analyze Particles` function. See 5.2(g).

11. Remaining white pixels groups that are separated just by a few black pixels are merged together using the `Binary > Close-` function. See Fig. 5.2(h).

12. Finally, remaining white pixels groups smaller than 300 pixels are eliminated, using the `Analyze Particles` function. See Fig. 5.2(i).

Some of the variables of this macro may need to be adjusted depending on the quality of the video (some videos are a bit blurred - it is not easy to focus a Schlieren image), the thickness of the flame front, lighting conditions, etc.

More theoretical information about these image-processing operations can be found in the ImageJ User Guide [22] and in Gonzalez et al. [23].

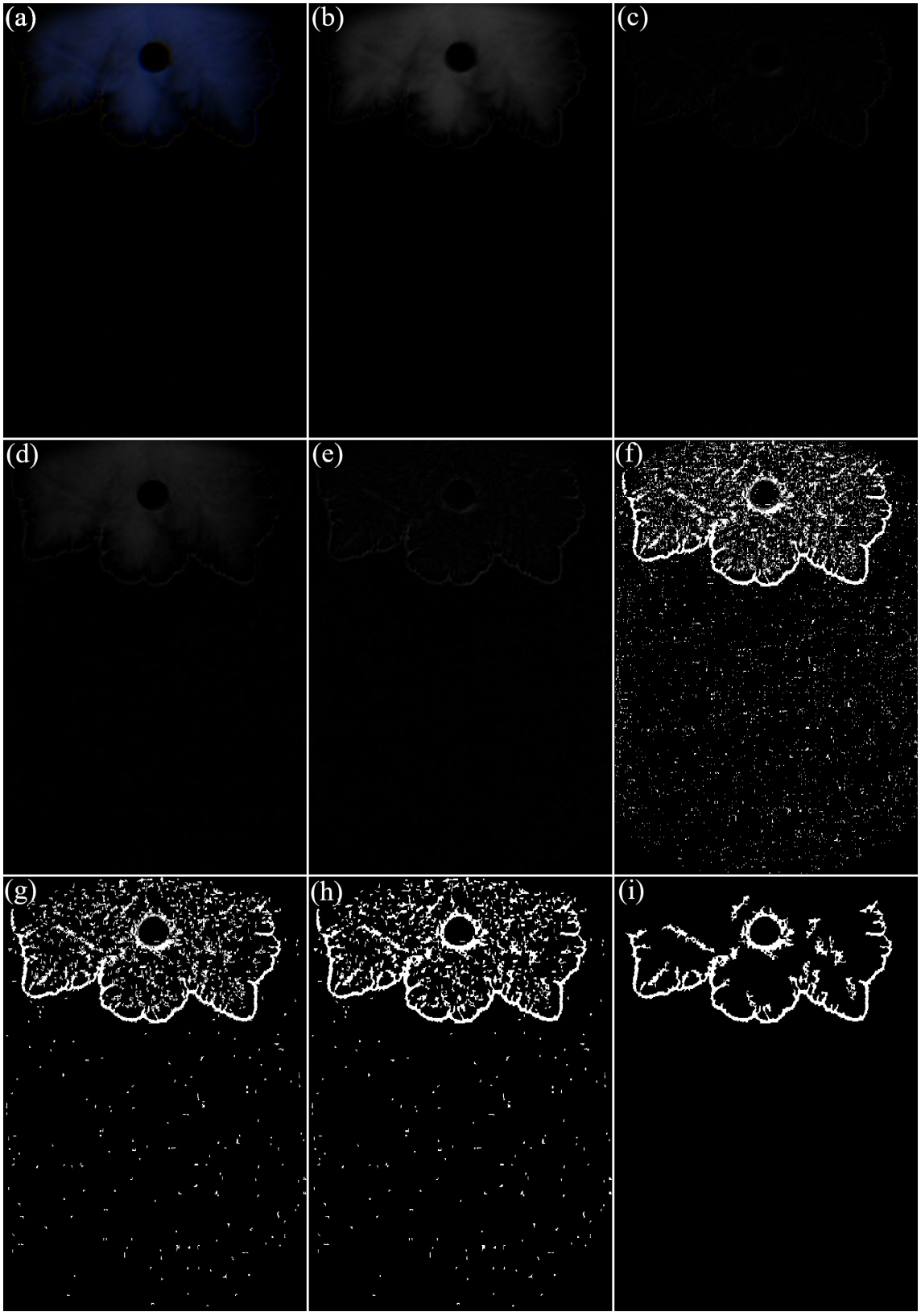

Fig. 5.2. Image processing steps. (a) Subtraction of the original image to the first one. (b) Conversion to grayscale. (c) Result of background subtraction. (d) Red channel of image (a). (e) Sum of images (d), with background subtracted, and (c). (f) Binarization of image (e), with threshold value 4. (g) Elimination of white particles smaller than 10 pixels. (h) Morphological closing. (i) Elimination of white particles smaller than 300 pixels.

5.2. Useful Information Extraction

The next step is to obtain relevant numerical data (flame front mean position, speed, and length) from the processed images. To do so, a Matlab program ans several functions have been developed and implemented. The general procedure is as follows:

1. If the white flame front does not reach the lateral edges of the image, which is the case most of the times, a horizontal white 1-pixel thick line is drawn on both sides of the image, as an extension of the flame front. This is necessary to account for the segments of the flame front that cannot be seen in the upper and lower parts of the image, due to the roundness of the visualization area. The result of this operation is shown in Fig. 5.3(a).

2. In each pixel column just the bottom-most white pixels are kept, while the others are made black. Any gaps in the flame front, i.e., columns with no white pixels, are filled by interpolating the positions of the surrounding pixels. Outliers, which are usually due to noise, are also replaced. As a result, a black picture is obtained, with just one white pixel in each column. The result of this operation is shown in Fig. 5.3(b).

3. Flame front length is estimated by assuming that the positions of the white pixels are cartesian coordinates of points of a line. First, the distance between every pair of such points is calculated, and then all these distances are summed up. Distances on the image can be related to real distances by proportionality with the width of the combustion chamber: 200 mm are 670 pixels.

4. The mean position of the flame is estimated by making all the black pixels *above* the white pixel in each column white, so that the burnt area is white, and the unburnt area is black, as shown in Fig. 5.3(c). Then, the burnt area is divided by the width of the channel, yielding the mean position of the flame front with respect to the upper edge of the image.

   To estimate the absolute position of the flame front in the chamber, the small black circles seen on the original images are used as reference. These circles are the shadow of three screws placed on one of the combustion chamber faces (see. Fig. 5.1), and they are known to be located at 200 mm, 550 mm, and 900 mm respectively from the top end of the chamber.

5. Once the flame position has been calculated for all the images of an experiment, the propagation speed can be easily found by calculating the numerical gradient of the position.

6. In order to assess the oscillation frequencies, Fourier spectra are plotted for both the calculated flame speed and pressure signal. Gaps in the speed data (due to

the different trials for each experiment) are filled with a `pchip` interpolation, as recommended by Trauth [24].

This procedure is based on the algorithms developed and implemented by Palacios-Mambrilla [8], for a similar application.

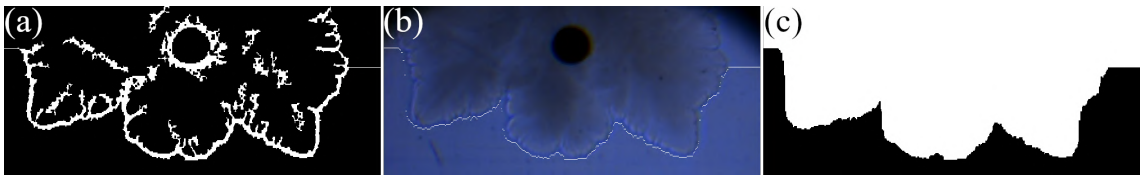

Fig. 5.3. Image manipulation with Matlab (detail). (a) Image from Fig. 5.2(i), with "closed" sides. (b) Superposition of the bottom-most white pixels from image (a) and the original image. (c) Burnt area.

One of the main drawbacks of this procedure is that it obtains the burnt area as the projection of the flame front from the bottom of the image. As a consequence, if the flame front "wraps" (i.e., if the flame front intersects a vertical straight line on the image more than once), part of the flame front is lost. For example, that is what happens on the right side of the images in Fig. 5.3. However, this problem is not frequently observed in the analyzed images, and the error is not expected to be relevant.

Another issue is that the results are often altered by the presence of the small black circles on the images. Usually, when the flame front crosses the black circle on an image, it results in a gap in the flame front on the binary image. Additionally, the ImageJ macro algorithm detects part of its contour as the flame front.

Not all the available videos are rigorously analyzed here. Not for all experiments all the three videos have been recorded, and some variables in the macro need to be adjusted before each run, depending on the particular case. Analyzing all the 102 videos would be extremely time-costly, and is not indispensable. For this reason, the main sources of information about an experiment is pressure signal analysis and visual inspection of the video, and image analysis is used just in some representative cases to confirm coupling and determine the magnitude of flame speed and length.

6. RESULTS AND DISCUSSION

Fig. 6.1 is a condensed summary of the results of the performed analysis. It shows the different instabilities observed in the combustion chamber at given equivalence ratio and chamber geometry conditions. Experimental data are available for 102 discrete points, but clear tendencies are observed among them, so approximate regions enclosing similar phenomena can be drawn.

In this chapter, detailed qualitative and quantitative characteristics of each of these regions are presented, as well as the objective criteria followed to determine the boundaries between them.

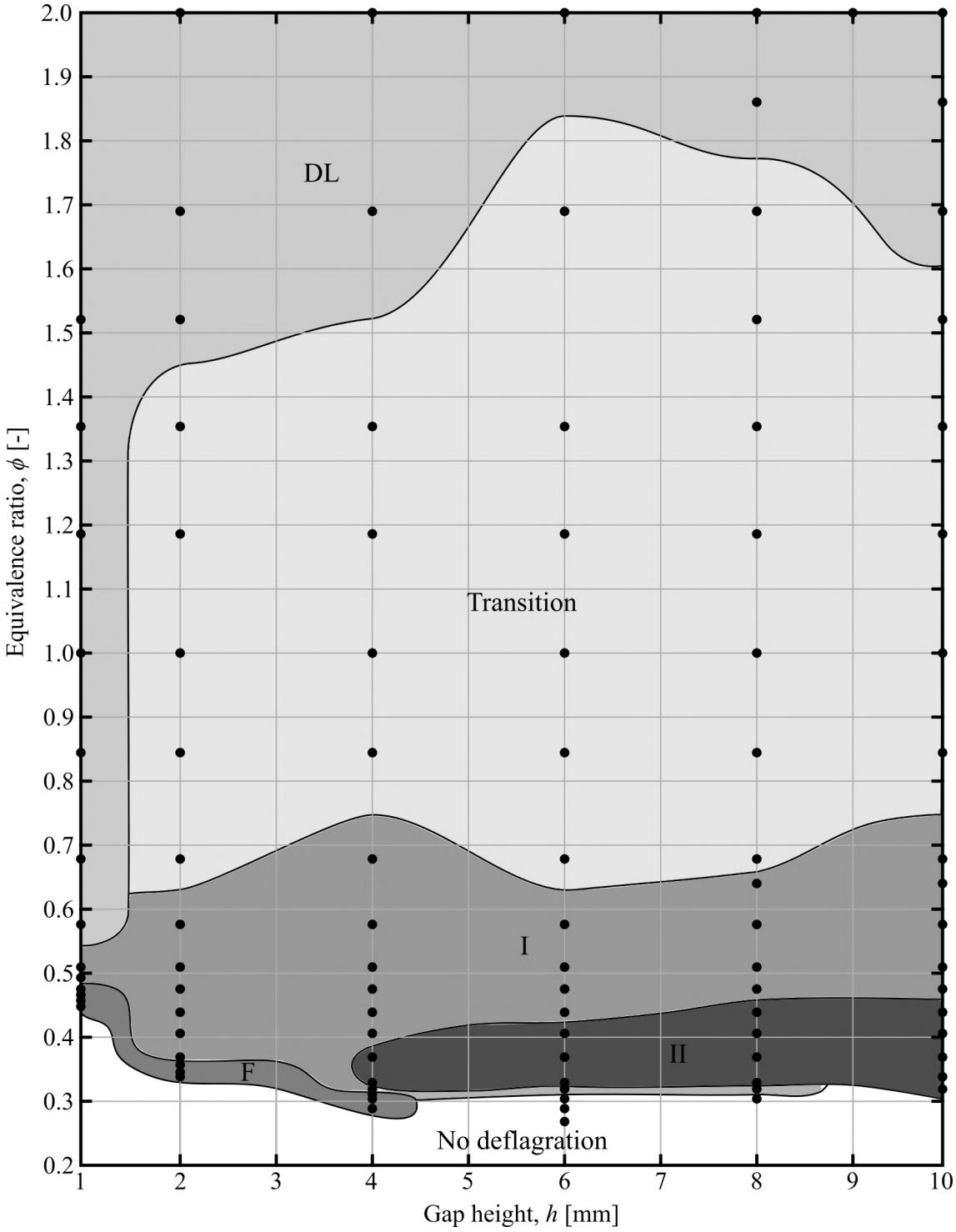

Fig. 6.1. Instabilities map. Each region represents a different kind of flame instability observed in the combustion chamber at given equivalence ratio and chamber thickness conditions. The black dots mark the 102 points for which actual data are available. DL: Darrieus-Landau. I: Primary thermoacoustic. II: Secondary thermoacoustic. F: Fractal.

6.1. Parametric Study

As it has already been discussed, the main source of information about the experiments, used to identify the different regions in Fig. 6.1, is the over-pressure data. Fig. 6.2 shows how the semi-amplitude and the dominant frequency of the acoustic waves vary with hydrogen concentration in the mixture for the different chamber thicknesses.

Amplitude variation follows a similar trend for all thicknesses, reaching however different maximum values. Except for $h = 10$ mm, the maximum over-pressure in the chamber right above the flammability limit is significantly lower than 1 kPa, and the instability observed in this region is the primary thermoacoustic one for chamber thickness of 6 mm or higher, and fractal for thicknesses of 4 mm or lower. The amplitude grows fast with equivalence ratio (except for $h = 1$ mm and 2 mm), and the point at which it reaches 1 kPa is assumed to be the boundary between primary and secondary regimes.

The presence of primary acoustic instabilities for mixtures leaner than the secondary ones, is only reported by [1].

At around $\phi = 0.45$ (13% vol. H_2), the maximum over-pressure falls below 1 kPa again, marking the transition back to the primary thermoacoustic regime. This region extends up to around $\phi = 0.7$ (20% vol. H_2). At this point the oscillations increase again, reaching the absolute maximum around the stoichiometric conditions in most of the cases. For $h = 6$ mm it occurs at $\phi = 0.68$ (20% vol. H_2), and for $h = 4$ mm there is a plateau between $\phi = 0.85$ (25% vol. H_2) and $\phi = 1.35$ (40% vol. H_2). This fact indicates that acoustic dissipation is minimum around stoichiometric conditions.

This region, in which the over-pressure is larger than 1 kPa, is the transition region. Finally, the oscillations fall once more down to nearly 0. At this point DL instability becomes the only observed instability.

Chamber thickness of $h = 1$ mm is a special case. Δp never exceeds 0.2 kPa, and the only instabilities observed by visual inspection of the videos are DL, thermodiffusive, and fractal. Some small oscillations are also detected around $\phi = 0.50$ (15% vol. H_2). In this case, the criterion to distinguish primary thermoacoustic from DL regions is based on the oscillation frequency: when it drops suddenly, DL becomes the dominating instability.

As it can be seen in Fig. 6.2(b), the rule of thumb is that the dominant frequency increases with chamber thickness, and does not vary a lot with equivalence ratio. Actually, closer inspection reveals a more sophisticated behavior. Regardless of the chamber thickness, the frequency for lean mixtures is about 79-90 Hz. It increases roughly linearly with equivalence ratio up to a maximum point, and then drops suddenly. This maximum value is higher for thicker chambers (250 Hz for 10 mm, 190 Hz for 8 mm, 130 Hz for 6 mm, and 100 Hz for 4 mm).

In a very thin chamber, however, the frequency evolves in a different way. For $h = 2$ mm, the frequency is nearly constant (60-75 Hz). For $h = 1$ mm, it is also nearly

constant (~20 Hz), except for the narrow interval around $\phi = 0.49$ (14% vol. H_2), corresponding to the thermoacoustic instability region.

Actually, for all thicknesses (except 1 mm), the frequency is about 80 Hz around $\phi = 0.34$ (10% vol. H_2). For $h = 10$ mm, the frequency increases with ϕ, reaching the maximum (250 Hz) at $\phi = 0.85$ (25% vol. H_2).

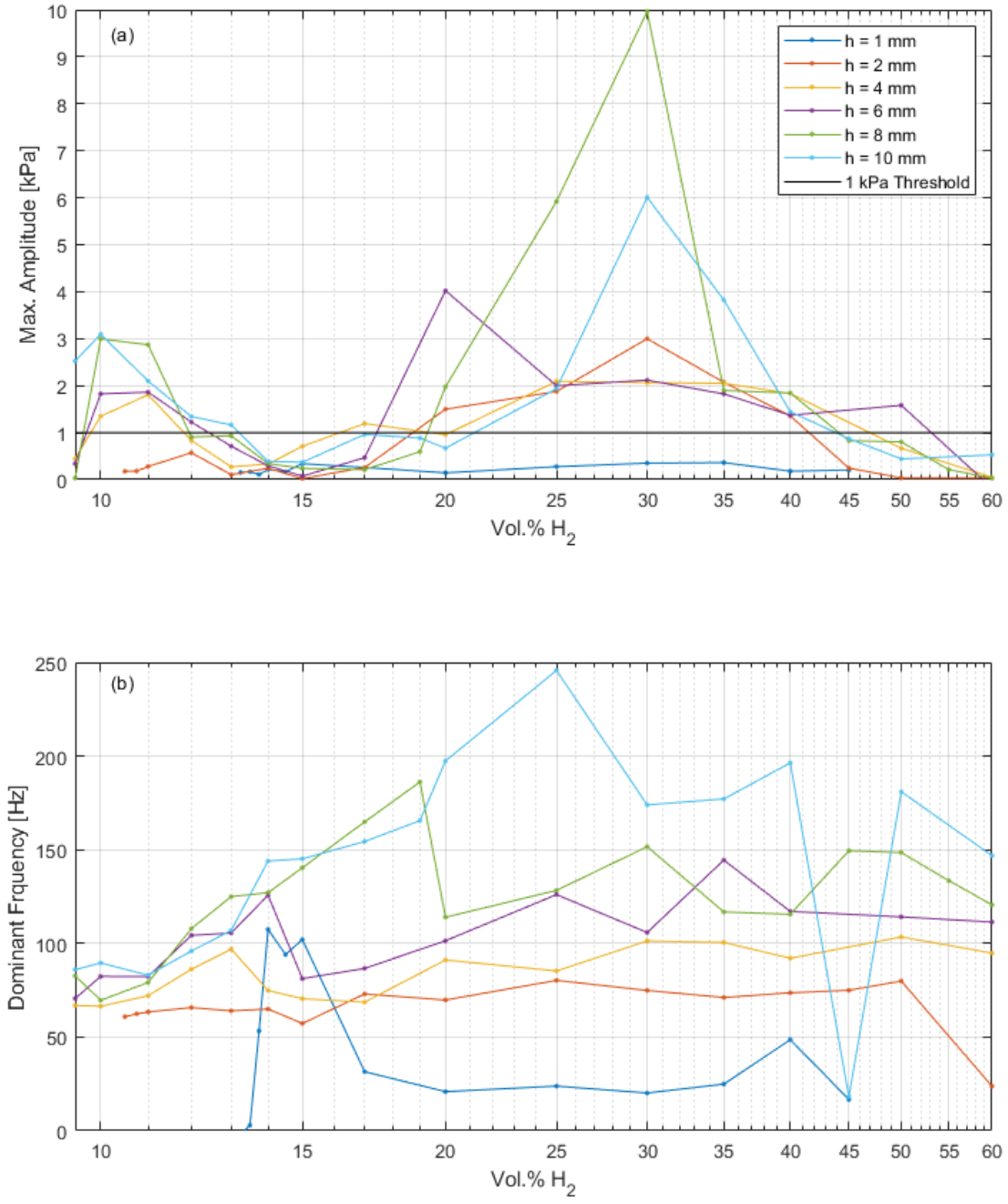

Fig. 6.2. (a) Variation with hydrogen volume fraction of maximum pressure oscillation semi-amplitude. (b) Variation with hydrogen volume fraction of pressure oscillation frequency.

6.2. Darrieus-Landau Instability Region

For very rich mixtures, the dominating instability is the Darrieus-Landau instability. The experiment with $h = 10$ mm and $\phi = 2$ (60% vol. H_2), which is considered representative, is described in detail in this section.

Fig. 6.3 shows the evolution of the flame in the chamber. The flame front is clearly curved during the whole process, presenting cells much larger than the flame front thickness. This structure is characteristic of the DL instability.

Fig. 6.4 shows the quantitative results of the analysis. The flame position evolution shows a linear trend. The middle segment is shifted to the left with respect to the other two, possibly due to a faster ignition and/or other random factors. Some fluctuations are observed in the flame speed evolution, which are mainly due to the variation of the flame front shape, especially formation of cusps. Note the peak at the very beginning, right after ignition. This peak corresponds to the relatively larger separation of the flame fronts at 0.010 s and 0.025 s in Fig. 6.3.

The over-pressure in the chamber presents small oscillations, that slowly grow in time reaching a maximum of 0.3 kPa. The irregularities observed around 0.27 s are caused by the flame front reaching the pressure probe at the end of the chamber. After that, the oscillations die away.

The flame length varies between 0.25 m and 0.35 m. The peak at the beginning is due to the fact that, short after ignition, the right part of flame front is almost vertical and the cells are smaller. Approximately from 0.1 s to 0.15 s the flame is observed to be flatter (see Fig. 6.3), and so the flame length is lower.

The Fourier spectrum analysis shown in Fig. 6.5 indicates that there is flame-pressure coupling at the end of the combustion process, at approximately 150 Hz.

For the case shown in Figs. 6.3 - 6.5, i.e., $h = 10$ mm and $\phi = 2.0$, the heat loss parameter Δ can be computed using Eq. 2.1 and data from Table 4.1:

$$\Delta \sim \left(\frac{\delta_T}{h}\right)^2 = \left(\frac{0.071\,\text{mm}}{10\,\text{mm}}\right)^2 \approx 1.2 \times 10^{-6} \ll 1.$$

So heat losses by wall conduction are expected to be negligible. On the other hand, according to Eq. 2.2, the acoustic dissipation losses are:

$$\frac{t_a}{t_d} \sim \frac{2\nu L}{ch^2} = \frac{2(15 \times 10^{-6}\text{m}^2\,\text{s}^{-1})(0.95\,\text{m})}{(695\,\text{m}\,\text{s}^{-1})(0.01\,\text{m})^2} \approx 4.1 \times 10^{-4} \ll 1.$$

So acoustic waves have enough time to interact with the flame before they are dissipated by viscosity in the boundary layer. Therefore heat losses and viscous dissipation do not play a significat role in this case.

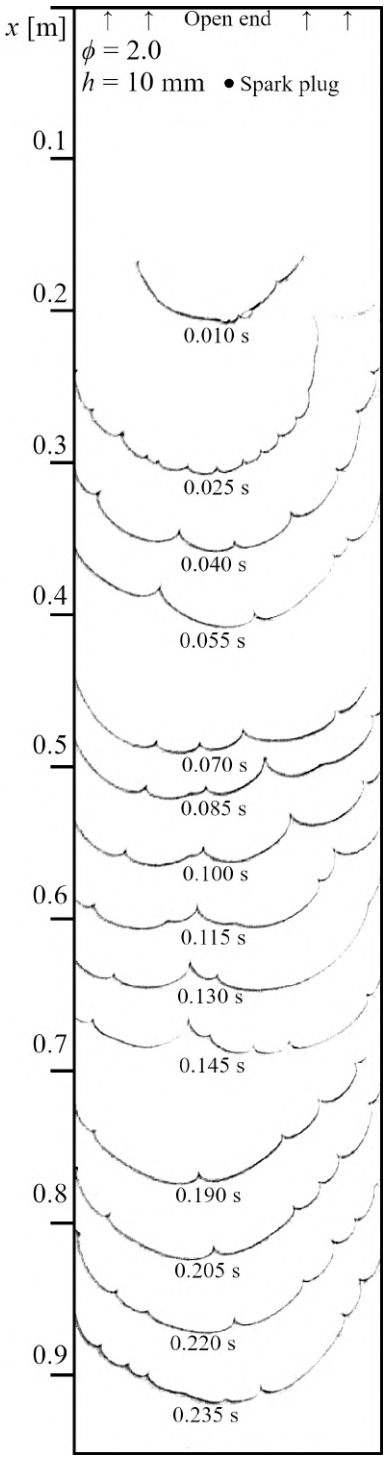

Fig. 6.3. Superposition of images selected from the videos corresponding to the experiment with h = 10 mm and ϕ = 2 (60% vol. H_2), at 0.015 s intervals. The images up to 0.055 s are taken from the top visualization area video, 0.070 s - 0.145 s from the middle one, and 0.190 s - 0.235 s from the bottom one.

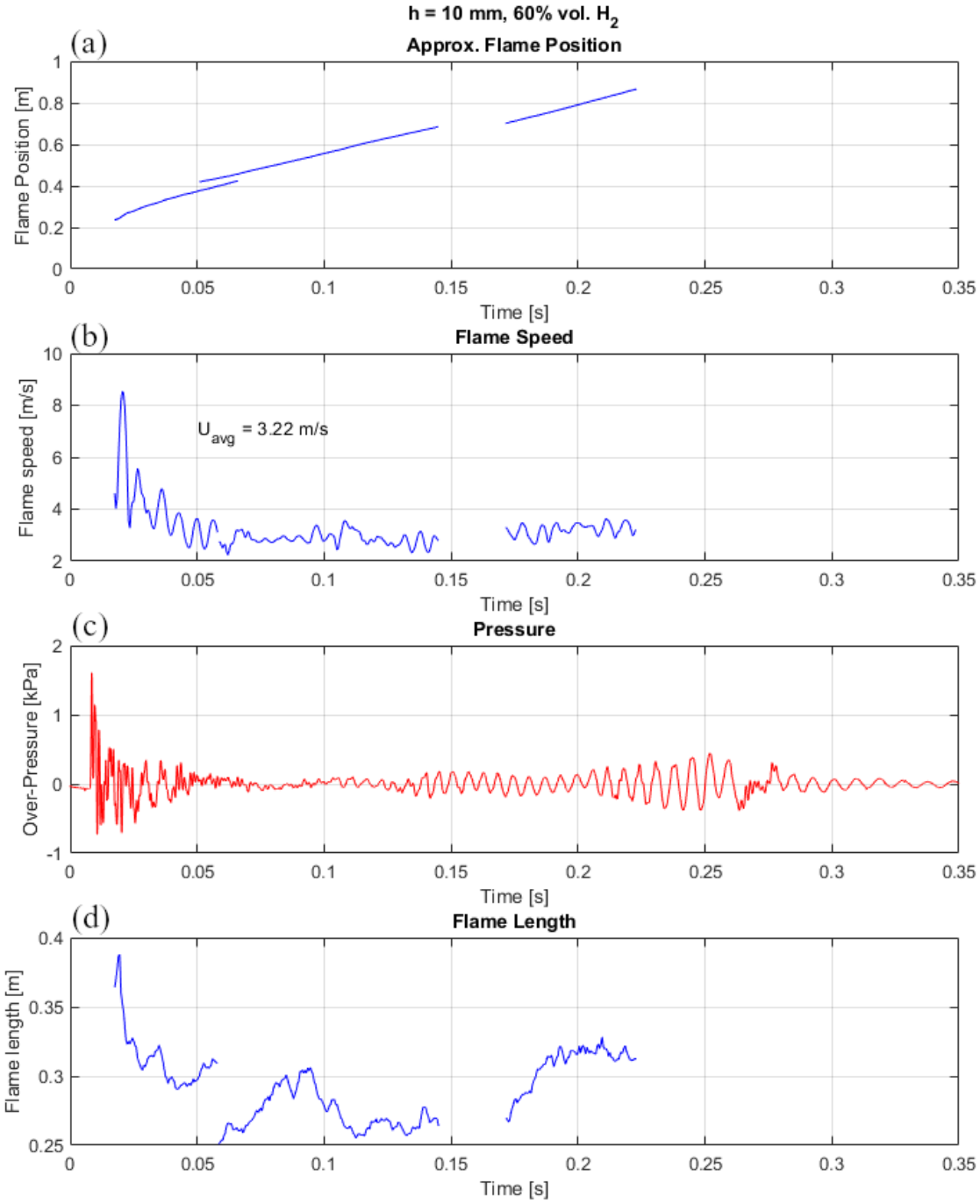

Fig. 6.4. Numeric results of the experiment with $h = 10$ mm and $\phi = 2$ (60% vol. H_2). (a) Evolution of flame front mean position in the chamber. (b) Evolution of flame front mean propagation speed. (c) Evolution of pressure in the chamber. (d) Evolution of flame length.

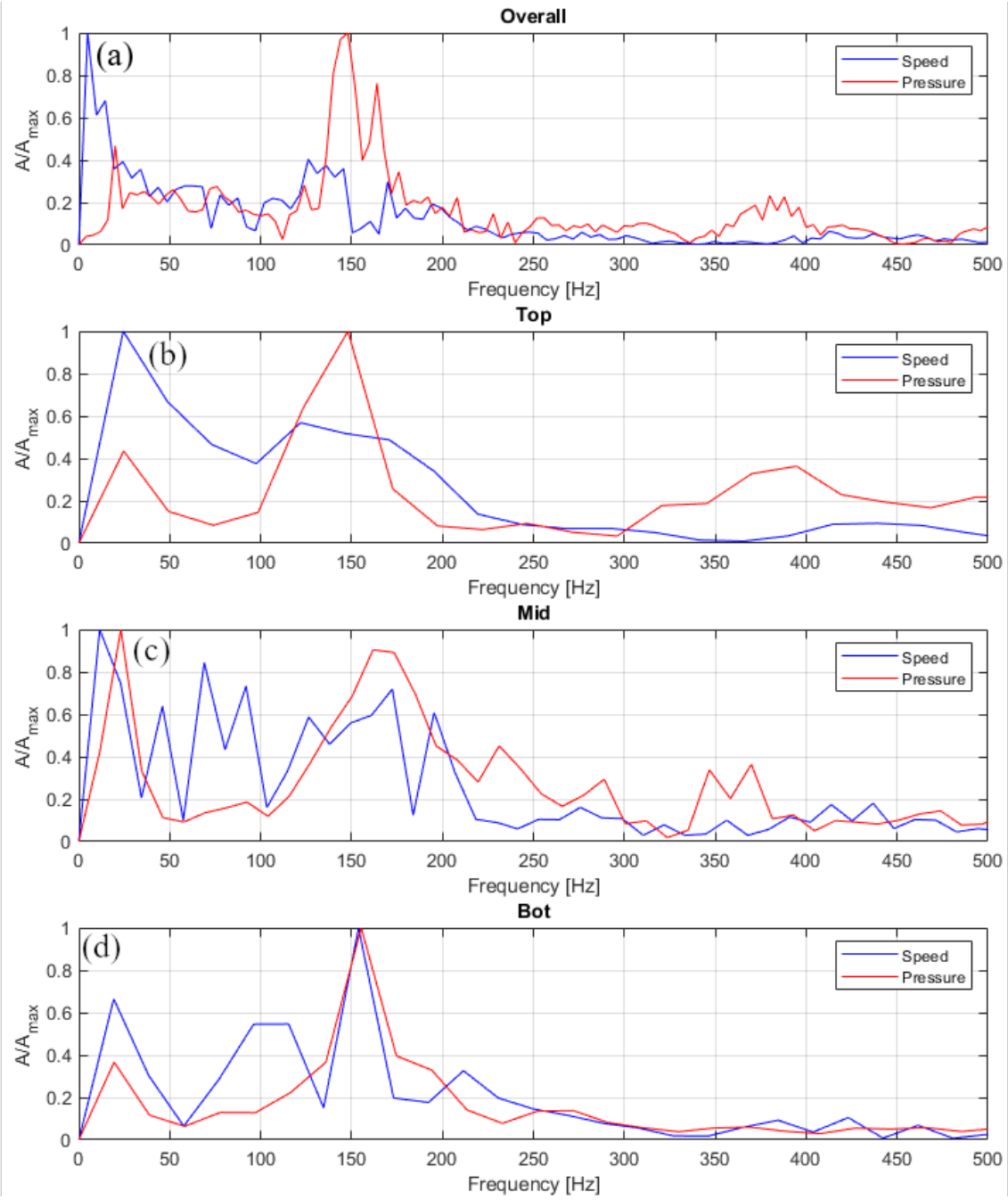

Fig. 6.5. Fourier spectra of the speed and pressure signals of the experiment with $h = 10$ mm and $\phi = 2$ (60% vol. H_2). (a) Spectrum of the entire signals. (b) Spectrum of the part corresponding to the top visualization area. (c) Spectrum of the part corresponding to the middle visualization area. (d) Spectrum of the part corresponding to the bottom visualization area.

6.3. Transition Region

There is a transition region for mixtures of equivalence ratio roughly between 0.7 and 1.4 (20% and 50% vol. H_2), and chamber thickness larger than 1 mm. The flame presents features characteristic to different instabilities, and cannot be categorized as just a single one of them.

In this region, the maximum over-pressure in the chamber is at least 1.5 kPa, reaching to 10 kPa in one extreme case ($h = 8$ mm and $\phi = 1.0$ (30% vol. H_2)). In general, the frequency of these oscillations is in the range 100 Hz - 250 Hz. As for the structure of the flame front, both DL and thermodiffusive instabilities are observed in most of this region, but as the equivalence ratio increases, the thermodiffusive ones become less important, and they completely dissapear around $\phi = 1.19$ (35% vol. H_2), i.e., when the Lewis number becomes larger than 1.

Although flame oscillations are also present, coupling is not as evident as in the thermoacoustic case. On the other hand, it should be noted that the average flame speed increases with equivalence ratio and the flame reaches the bottom of the chamber in less time. As a consequence, the variation of variables in the time domain is larger from one data point to another and the Fourier spectra in Fig. 6.8 are less accurate.

The experiment with $h = 6$ mm and $\phi = 0.68$ (20% vol. H_2), which is considered representative, is described in detail next.

Fig. 6.6 shows several snapshots from that experiment. DL and thermodiffusive instabilities are present: the flame front is wrinkled and very curved.

As it can be seen in Fig. 6.7(a), the overall trend of the flame propagation is linear, although flame oscillation are significant (Fig. 6.7(b)), reaching peak speeds of 6 m/s. In fact, these oscillations grow in time, as well as pressure oscillations (Fig. 6.7(c)). This fact suggest coupling exists. Besides, flame length is rather high, reaching up to 0.6 m in the final part (Fig. 6.7(d)). That confirms that the flame front is highly curved and wrinkled.

The sudden drop in flame speed and rise in flame length at approximately $t = 0.11$ s observed in Fig. 6.7(b) and (d), are due to the flame crossing the round screw shadow in the video.

Fig. 6.8 shows that the dominant frequency of the acoustic field is clearly distinguishable, but it significantly varies in time: first it is about 25 Hz, then it grows up to 300 Hz, and finally falls back to 100 Hz. The power associated to this last frequency is clearly much higher than the other two (Fig. 6.8(a)).

Power of the velocity field oscillations is distributed over a broader bandwidth. Even so, some similitude to the pressure spectra can be found, especially in the last part (Fig. 6.8(d)).

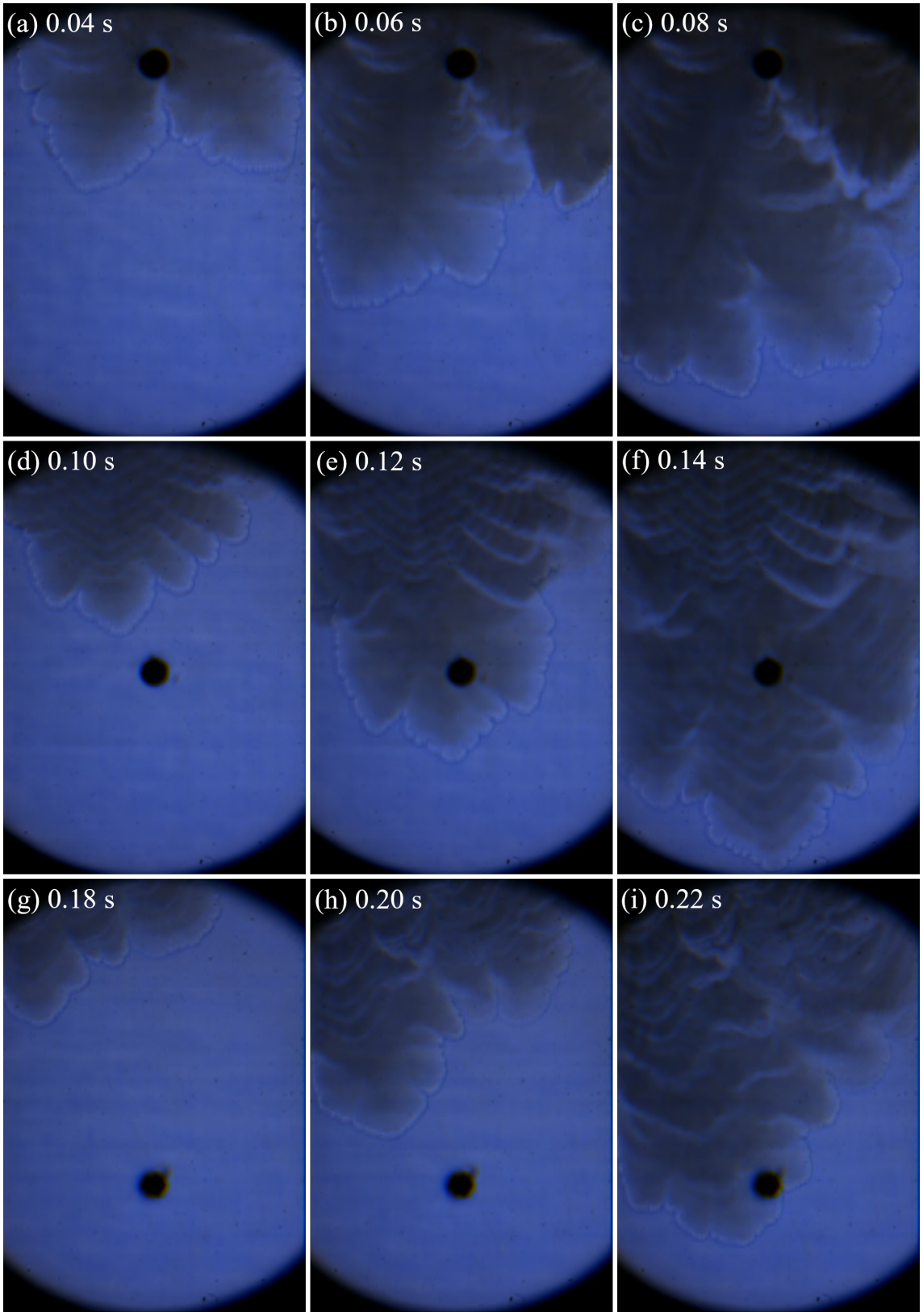

Fig. 6.6. Selection of images of the experiment with h = 6 mm and ϕ = 0.68 (20% vol. H_2).

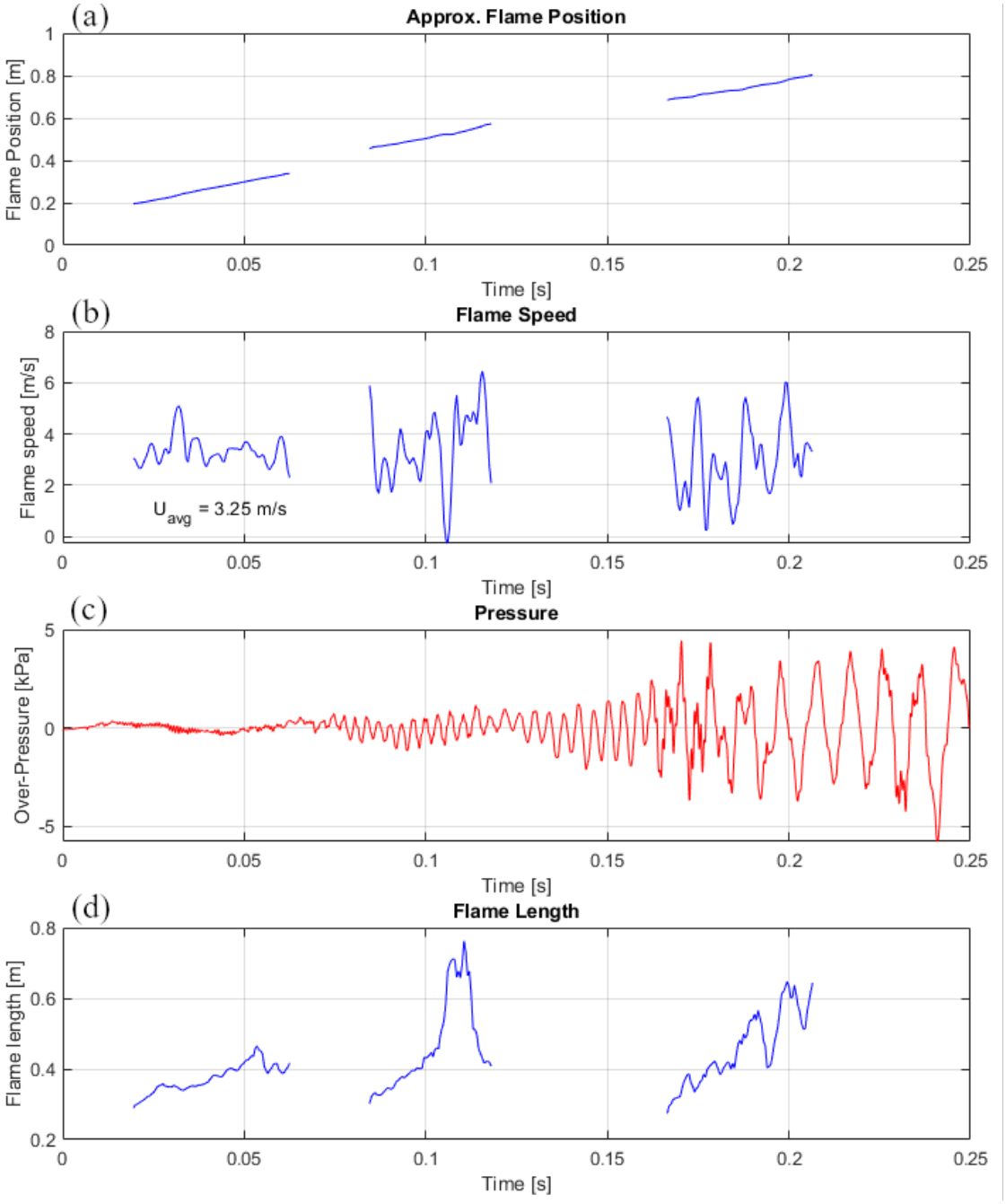

Fig. 6.7. Numeric results of the experiment with $h = 6$ mm and $\phi = 0.68$ (20% vol. H_2). (a) Evolution of flame front mean position in the chamber. (b) Evolution of flame front mean propagation speed. (c) Evolution of pressure in the chamber. (d) Evolution of flame length.

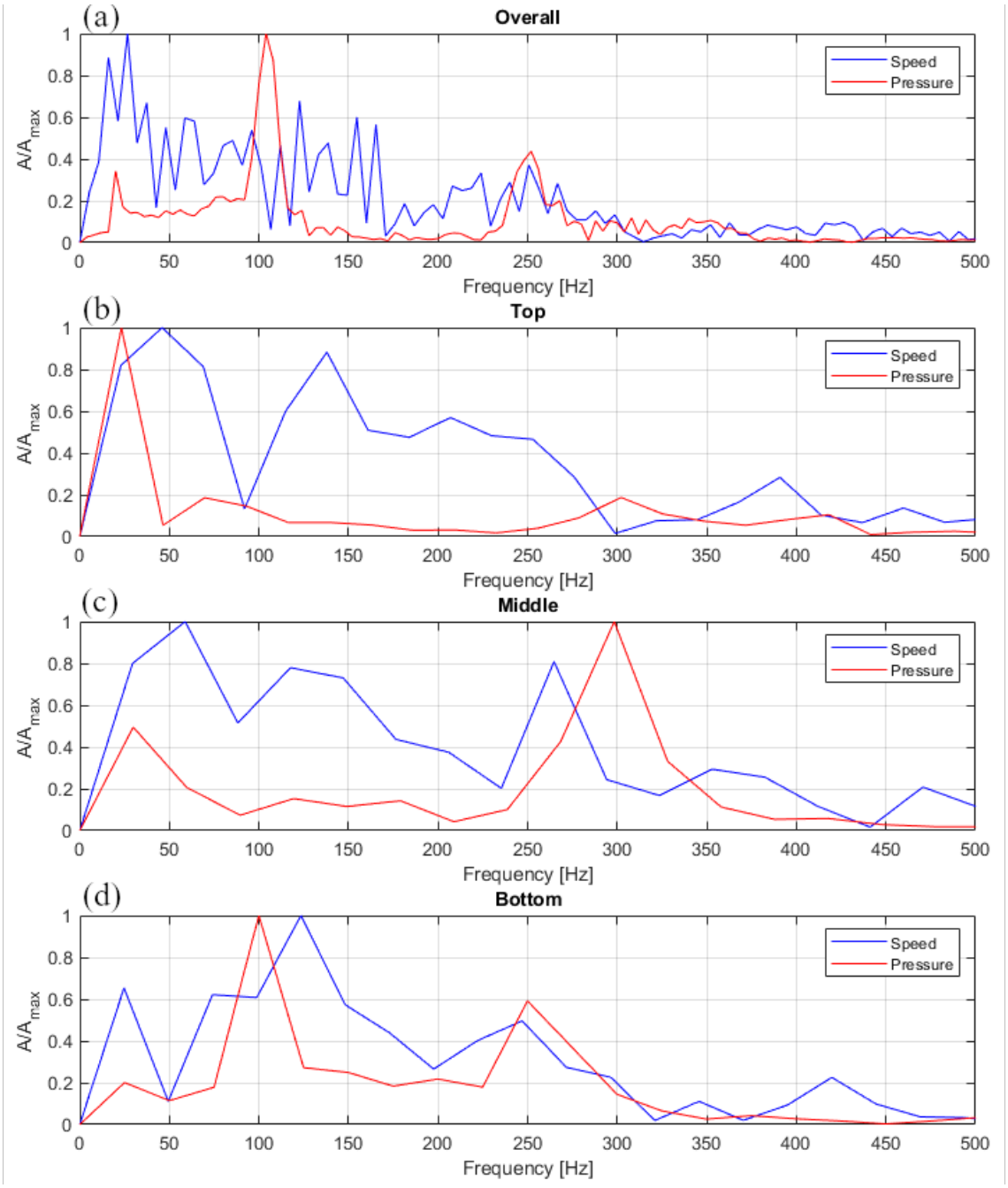

Fig. 6.8. Fourier spectra of the speed and pressure signals of the experiment with $h = 6$ mm and $\phi = 0.68$ (20% vol. H_2). (a) Spectrum of the entire signals. (b) Spectrum of the part corresponding to the top visualization area. (c) Spectrum of the part corresponding to the middle visualization area. (d) Spectrum of the part corresponding to the bottom visualization area.

6.4. Primary Thermoacoustic Instability Region

Primary thermoacoustic instability is characterized by flame oscillations coupled with the pressure waves in the chamber. The amplitude of these oscillations is not as big as in the secondary thermoacoustic instabilities. The criterion used here to distinguish between primary and secondary regimes, is the maximum over-pressure in the chamber: if it is lower than 1 kPa the instability is assumed to be primary.

The experiment with $h = 10$ mm and $\phi = 0.47$ (14% vol. H_2), which can be considered representative of this region, is described in detail in this section.

Fig. 6.10 shows the quantitative results of the analysis. As it can be observed in Fig. 6.10(a), the flame propagation follows a linear trend. Flame oscillations appear approximately at the midpoint of the chamber (Fig. 6.10(b)), together with an increase in amplitude pressure oscillations. This is in agreement with the observations made by Searby [13].

The flame length is roughly double the chamber width, due to the curved and wrinkled flame front. The valley at about 0.24 s is due to the "side-closing" procedure described in Section 5.2, point 1. In this region, the parts of the flame front are not visible on the images, due to the roundness of the visualization area. The straight lines artificially added on the sides of the image significantly reduce the flame length. The valley at 0.35 s is due just to temporary flattening of the flame front.

Spectral analysis, shown in Fig. 6.11, confirms that coupling exists. Oscillation frequency is in general between 100 and 150 Hz, and slightly varies in time.

For the case shown in Figs. 6.9 - 6.11, i.e., $h = 10$ mm and $\phi = 0.47$, the heat loss parameter Δ can be computed using Eq. 2.1 and data from Table 4.1:

$$\Delta \sim \left(\frac{\delta_T}{h}\right)^2 = \left(\frac{0.071\,\text{mm}}{10\,\text{mm}}\right)^2 \approx 5.0 \times 10^{-5} \ll 1.$$

So heat losses by wall conduction are expected to be negligible. On the other hand, according to Eq. 2.2, the acoustic dissipation losses are:

$$\frac{t_a}{t_d} \sim \frac{2\nu L}{ch^2} = \frac{2(15 \times 10^{-6}\text{m}^2\,\text{s}^{-1})(0.95\,\text{m})}{(695\,\text{m}\,\text{s}^{-1})(0.01\,\text{m})^2} \approx 4.1 \times 10^{-4} \ll 1.$$

So acoustic waves have enough time to interact with the flame before they are dissipated by viscosity in the boundary layer.

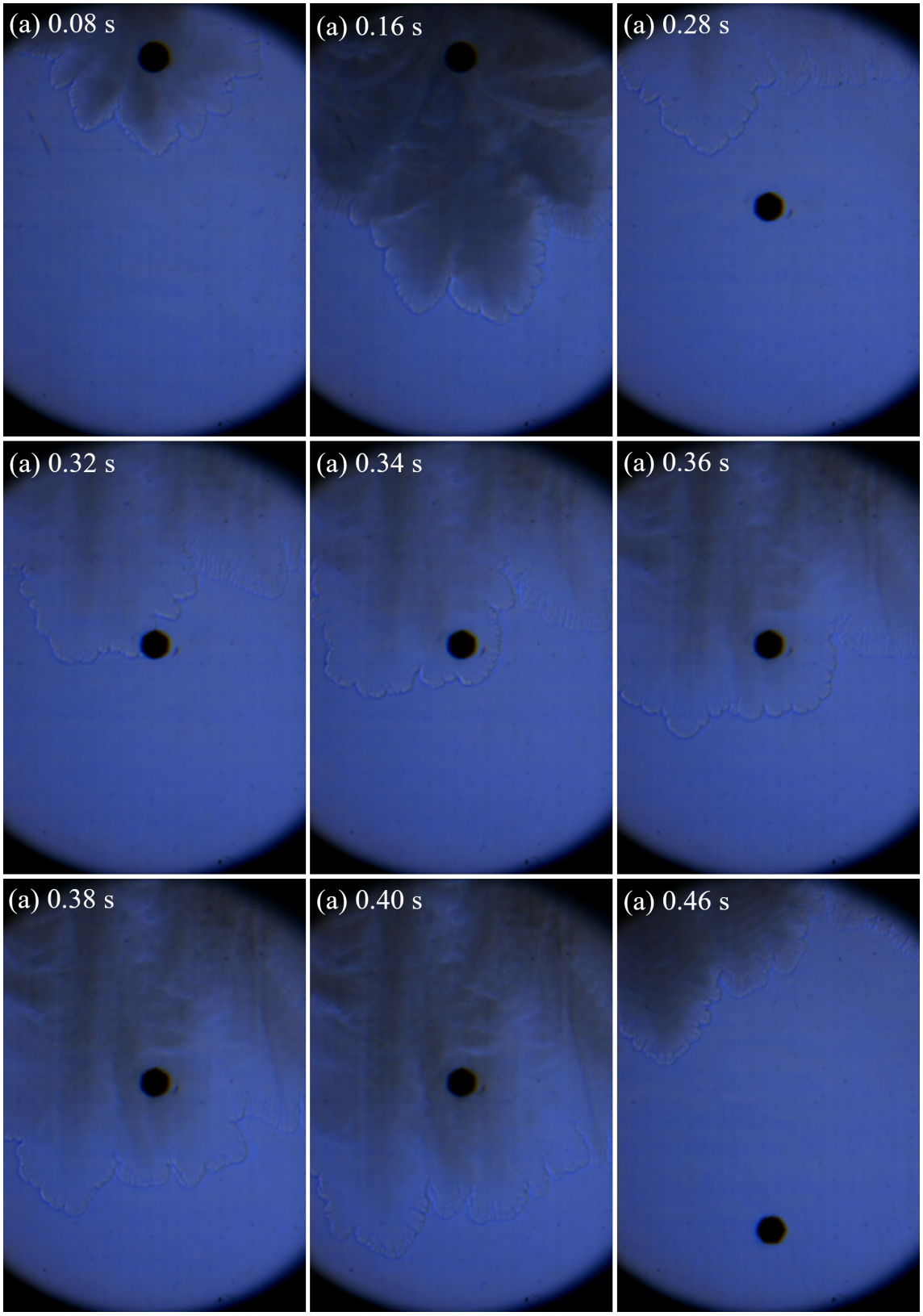

Fig. 6.9. Selection of images of the experiment with h = 10 mm and ϕ = 0.47 (14% vol. H_2).

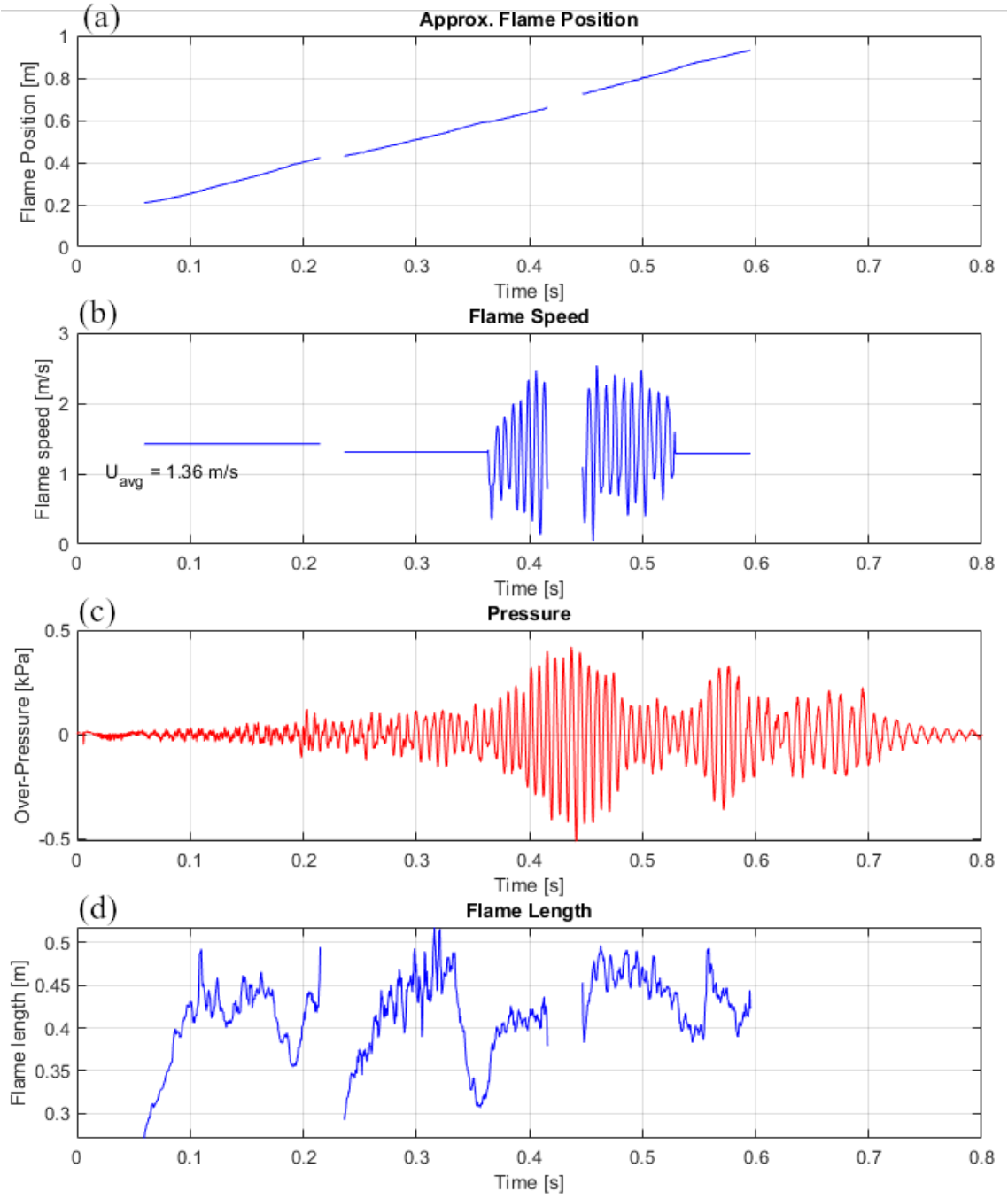

Fig. 6.10. Numeric results of the experiment with $h = 10$ mm and $\phi = 0.47$ (14% vol. H_2). (a) Evolution of flame front mean position in the chamber. (b) Evolution of flame front mean propagation speed. (c) Evolution of pressure in the chamber. (d) Evolution of flame length.

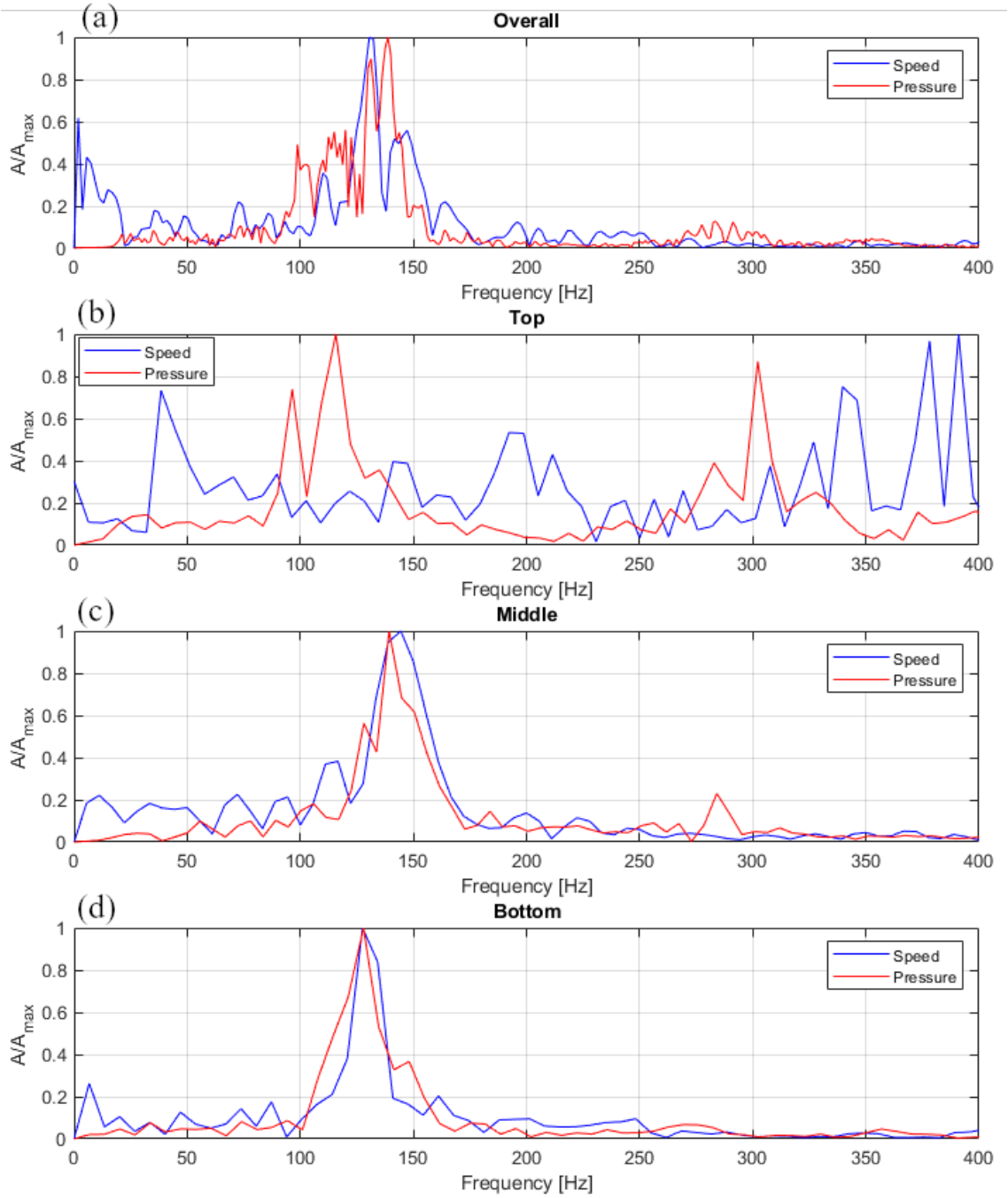

Fig. 6.11. Fourier spectra of the speed and pressure signals of the experiment with $h = 10$ mm and $\phi = 0.47$ (14% vol. H_2). (a) Spectrum of the entire signals. (b) Spectrum of the part corresponding to the top visualization area. (c) Spectrum of the part corresponding to the middle visualization area. (d) Spectrum of the part corresponding to the bottom visualization area.

6.5. Secondary Thermoacoustic Instability Region

Secondary thermoacoustic instability is characterized by flame and pressure oscillations significantly larger than in the primary regime. Here, a thermoacoustic instability is considered to be secondary when $\Delta p > 1$ kPa.

The experiment with $h = 10$ mm and $\phi = 0.34$ (10% vol. H_2), which can be considered representative of this region, is described in detail in this section.

Fig. 6.12 shows the appearance of the flame front during the different stages. At the beginning, the flame is curved and wrinkled (Fig. 6.12(a)), which are characteristic features of the DL and thermodiffusive instabilities, respectively. Soon, the oscillations stabilize the hydrodynamic effects, and the flame becomes flatter (Fig. 6.12(b)). Also, large finger-like cells are formed, which in some cases can be up to 25 mm wide. Toward the end of the combustion, the size of the cells and oscillations decrease again.

Several more subtle details can be observed in that Figure as well. In Fig. 6.12(a), the flame front seems to be composed of three triangular segments, which are roughly symmetrical. At the bottom-most part of these triangles (i.e., at the "vertex" of the triangle), a "slot" is observed. In other words, the "vertices" of the triangles are split in two thermo-diffusive cells. This feature resembles the double headed flame fronts observed in the fractal instability (e.g. see Fig. 6.15).

In Fig. 6.12(b), partial quenching of the flame front can be observed, which indicates that heat losses make the flame extinguish in these areas. This phenomenon is reported by [1]. In Figs. 6.12(d) and (g) the flame front is not clear, in fact closer inspection that there are several roughly parallel lines. This is due to cells forming also along the z direction, i.e., "perpendicular" to the images. This phenomenon is treated in [7].

Fig. 6.13 shows the quantitative results of the analysis. As it can be observed in Fig. 6.13(a), the flame propagation follows a linear trend at the beginning, but increases with the onset of the secondary oscillation. As it reaches the end of the combustion chamber it plateaus. Flame oscillations appear approximately at the midpoint of the chamber (Fig. 6.13(b)), together with an increase in amplitude pressure oscillations (Fig. 6.13(c)). This is in agreement with the observations made by Searby [13]. Peak speeds reach 6 m/s, while maximum over-pressure reach 3 kPa.

Flame length evolution is shown in Fig. 6.13(d) . As expected, the flame front is longer at the beginning, when it is curved. Then, its length oscillates as well, reaching larger peak values as the cells become smaller.

For the case shown in Figs. 6.12 - 6.14, i.e., $h = 10$ mm and $\phi = 0.47$, the heat loss parameter Δ can be computed using Eq. 2.1 and data from Table 4.1:

$$\Delta \sim \left(\frac{\delta_T}{h}\right)^2 = \left(\frac{0.182\,\text{mm}}{10\,\text{mm}}\right)^2 \approx 3.3 \times 10^{-4} \ll 1.$$

The heat loss parameter is one order of magnitude larger than in the primary regime example, but heat losses are still negligible. On the other hand, according to Eq. 2.2, the acoustic dissipation losses are:

$$\frac{t_a}{t_d} \sim \frac{2\nu L}{ch^2} = \frac{2(15 \times 10^{-6} \mathrm{m^2\,s^{-1}})(0.95\,\mathrm{m})}{(695\,\mathrm{m\,s^{-1}})(0.01\,\mathrm{m})^2} \approx 4.1 \times 10^{-4}.$$

Since the chamber thickness is the same as in the primary regime example, the characteristic times ratio does not change.

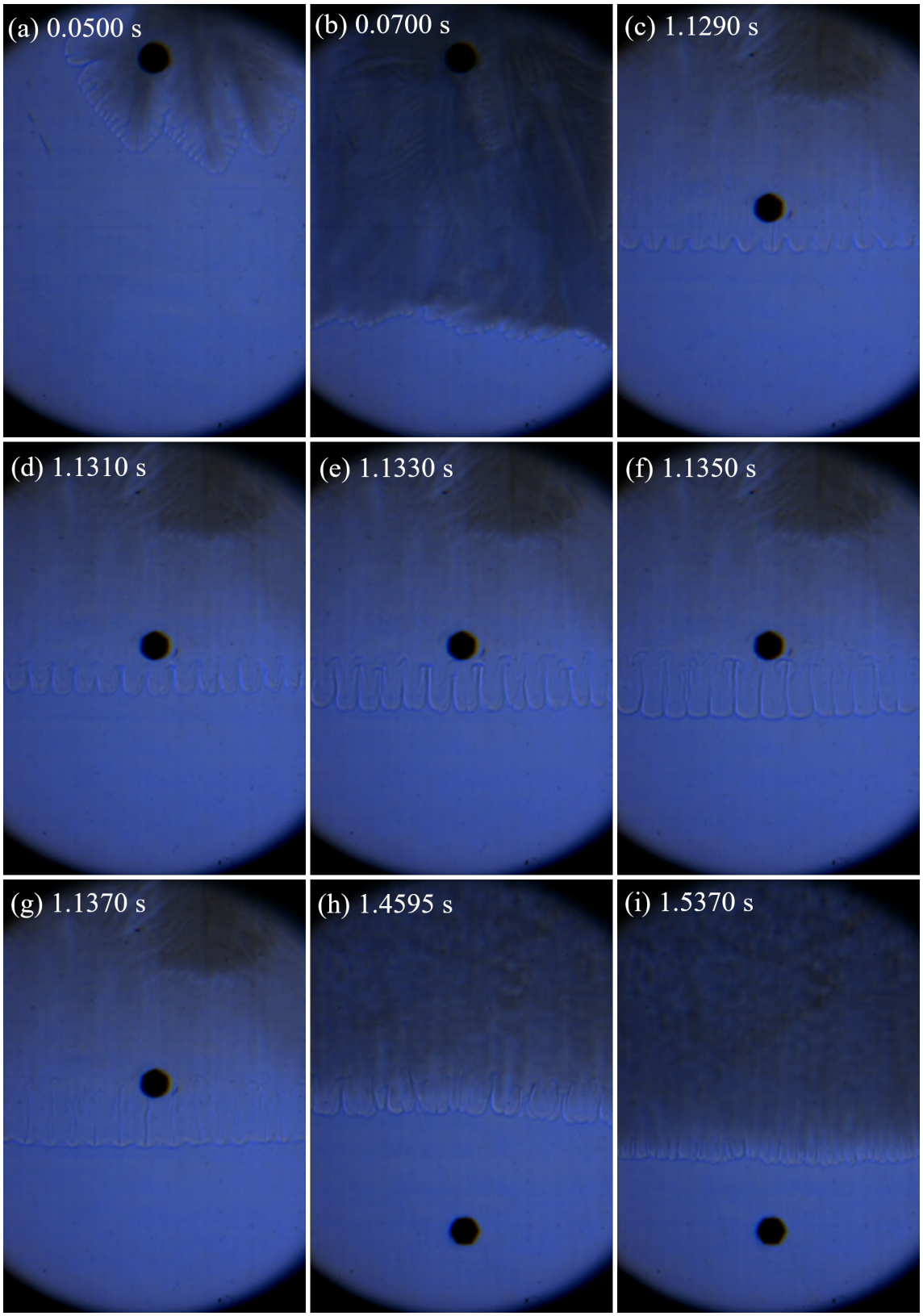

Fig. 6.12. Selection of images of the experiment with $h = 10$ mm and $\phi = 0.34$ (10% vol. H_2). (a) DL and thermodiffusive instabilities right after ignition. (b) Oscillations stabilize the DL instability, i.e., the flame front flattens. (c)-(g) Snapshots from a secondary instability oscillation cycle, with large finger-like cells. (h)-(i) Cells size and propagation speed decrease in the last part of the combustion.

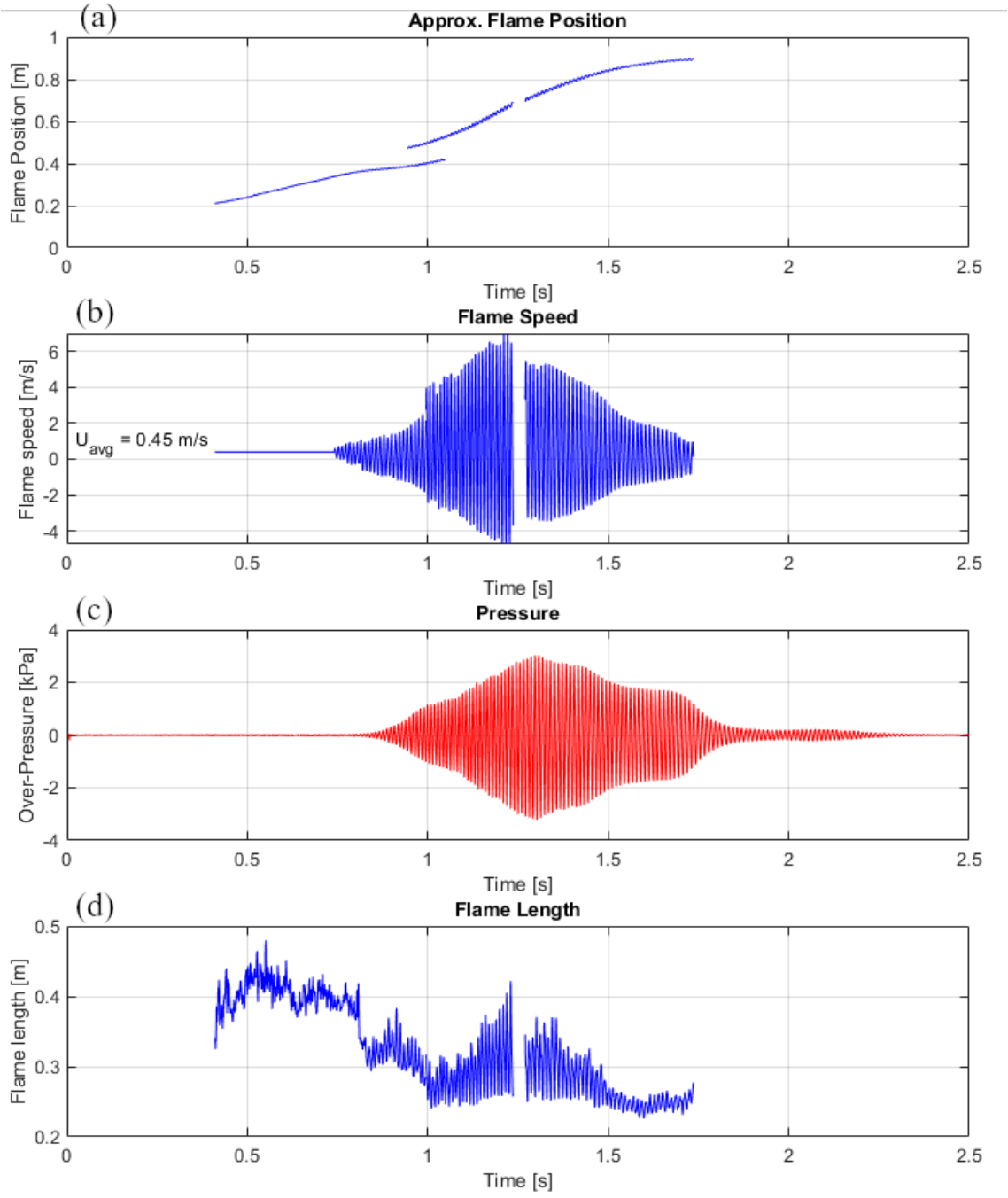

Fig. 6.13. Numeric results of the experiment with $h = 10$ mm and $\phi = 0.34$ (10% vol. H_2). (a) Evolution of flame front mean position in the chamber. (b) Evolution of flame front mean propagation speed. (c) Evolution of pressure in the chamber. (d) Evolution of flame length.

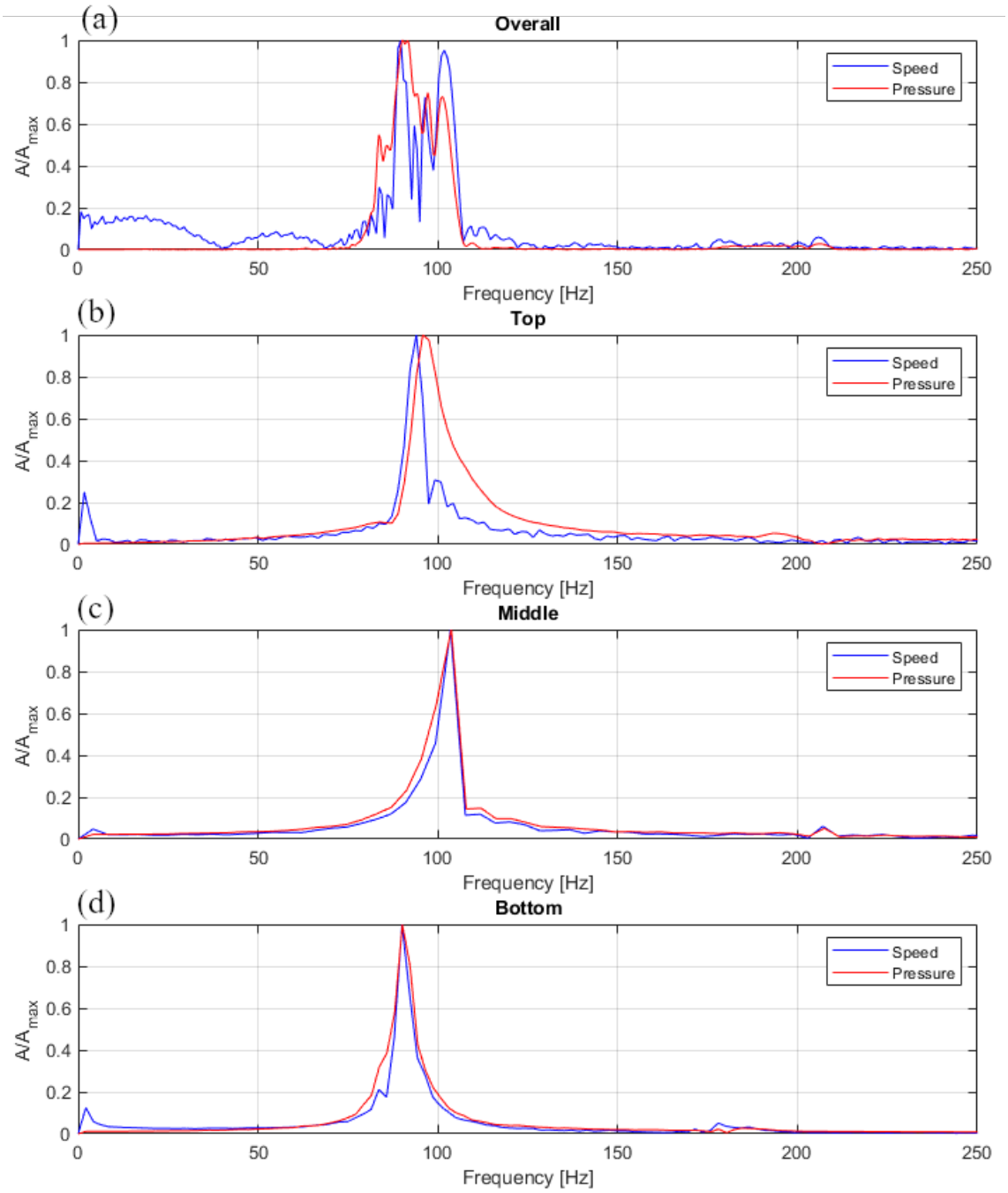

Fig. 6.14. Fourier spectra of the speed and pressure signals of the experiment with $h = 10$ mm and $\phi = 0.34$ (10% vol. H_2). (a) Spectrum of the entire signals. (b) Spectrum of the part corresponding to the top visualization area. (c) Spectrum of the part corresponding to the middle visualization area. (d) Spectrum of the part corresponding to the bottom visualization area.

6.6. Fractal Instability Region

Combustion of very lean mixtures (just above the flammability limit) in a very thin chamber (chamber thickness up to 4 mm) is a very peculiar case. Several tiny flame fronts appear, with a flame front length of the order of millimeters. Additionally, each of these fronts is divided in two symmetric halves or heads.

These small flame fronts tend to split and form smaller branches. As a result, a fractal-like structure is developed, somewhat resembling tree branches or leaves. In Fig. 6.15 the condensation trails left by the flame are clearly visible. The flame does not usually reach the bottom of the chamber, and part of the hydrogen remains unburnt.

Fig. 6.16 shows the measured pressure signal of the same experiment as Fig. 6.15. Very small oscillations can be observed at a frequency of 60 Hz.

For the case shown in Fig. 6.15, i.e., $h = 2$ mm and $\phi = 0.36$, the heat loss parameter Δ can be computed using Eq. 2.1 and the data from Table 4.1:

$$\Delta \sim \left(\frac{\delta_T}{h}\right)^2 = \left(\frac{0.153\,\text{mm}}{2\,\text{mm}}\right)^2 \approx 0.0059.$$

However, it should be noted that in this case the definition of this Δ parameter in Eq. 2.1 is not completely suitable, since the total flame front length is very small. Actual flame heat release is smaller than estimated, so heat losses are more important.

On the other hand, the acoustic dissipation losses are:

$$\frac{t_a}{t_d} \sim \frac{2\nu L}{ch^2} = \frac{2(15\times10^{-6}\text{m}^2\,\text{s}^{-1})(0.95\,\text{m})}{(695\,\text{m}\,\text{s}^{-1})(0.002\,\text{m})^2} \approx 0.010.$$

This value also confirms that viscous dissipation starts to be non-negligible in this region as well.

In some cases, small pressure oscillations are observed. The semi-amplitude and frequency of these oscillations (if any) is similar to the primary thermoacoustic regime ($\sim$ 0.1 kPa and 50-70 Hz). In some cases, the flame front is observed to oscillate in the videos as well. However, the image processing technique presented in this project is not suitable for such a complex flame structure, and coupling cannot be confirmed.

Also for this reason, the only criterion to identify fractal instability is by means of qualitative visual inspection of the videos.

Fig. 6.17 shows some particularly interesting cases. In Fig. 6.17(a), an upward propagating branch is observed. In Fig. 6.17(b), several fronts with a double head are observed to split apart. Fig. 6.17(c) shows the leanest mixture for which combustion is possible. At the very beginning, all the tiny flame fronts stick together (resulting in the gray "cloud" around the ignition port), later on some of them die and the others keep propagating separately.

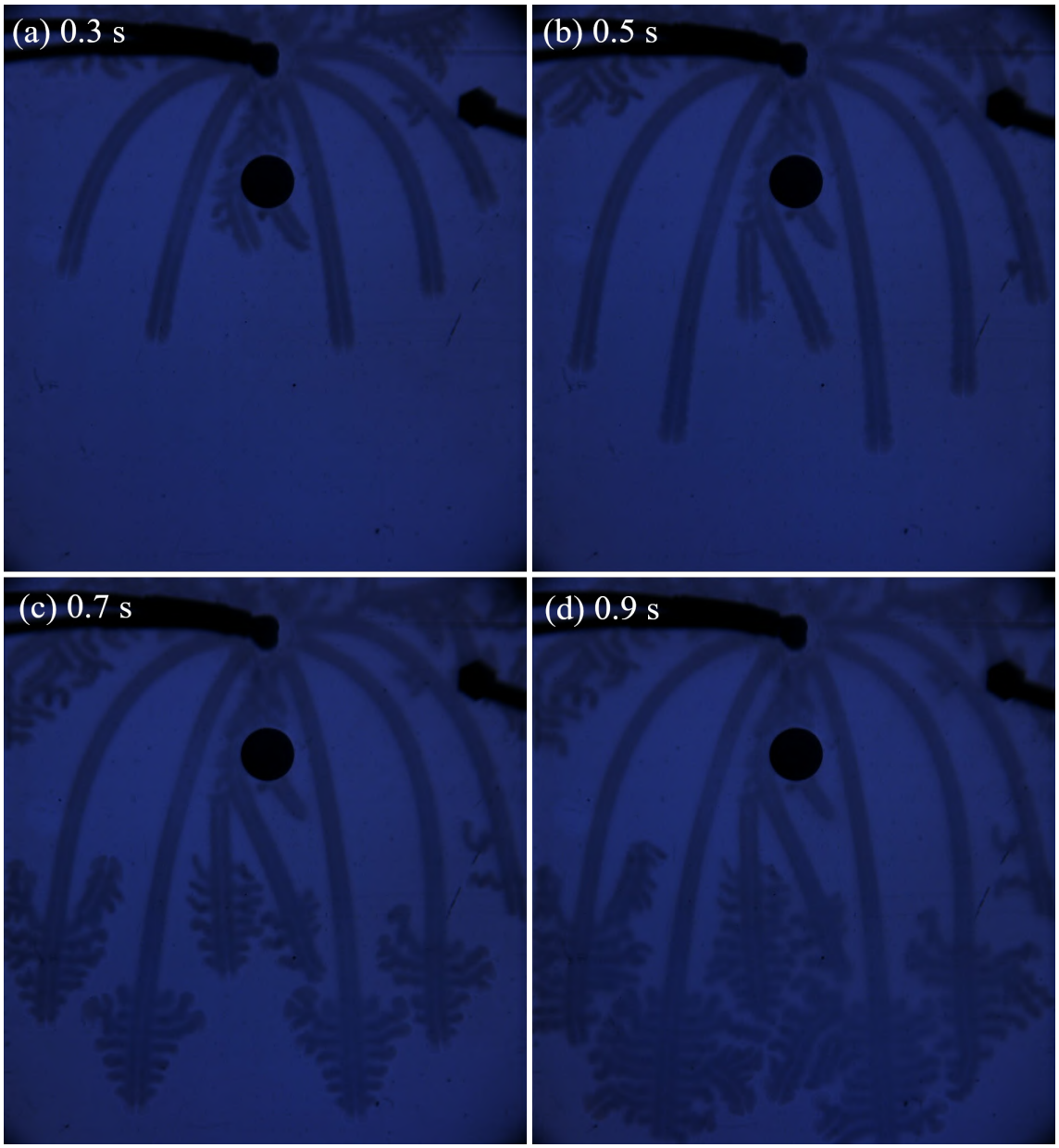

Fig. 6.15. Four images of the ignition region, with $h = 2$ mm and $\phi = 0.36$ (10.5% vol. H_2).

As the mixture gets richer, the flame fronts become wider and more irregular, until becoming a regular thermodiffusive instability. This intermediate state can be seen in Fig. 6.17(d).

This kind of instability is not found in the literature.

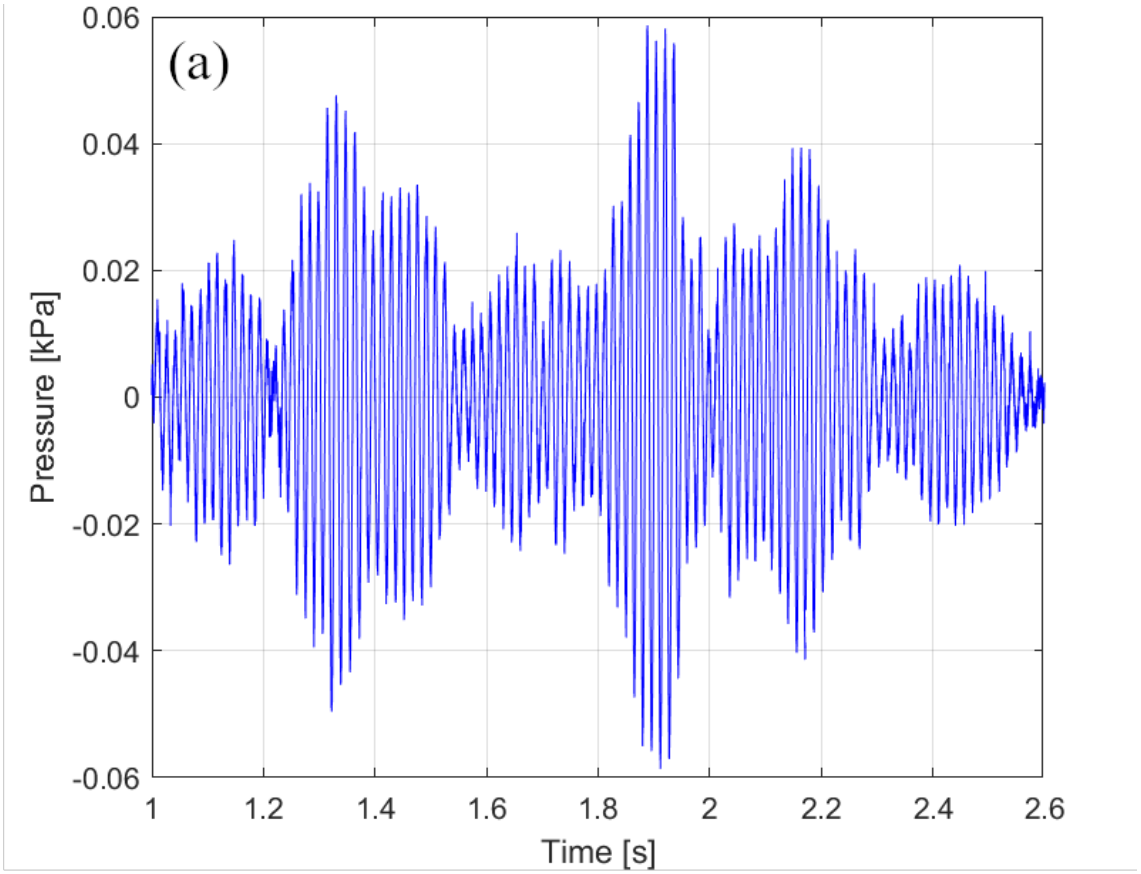

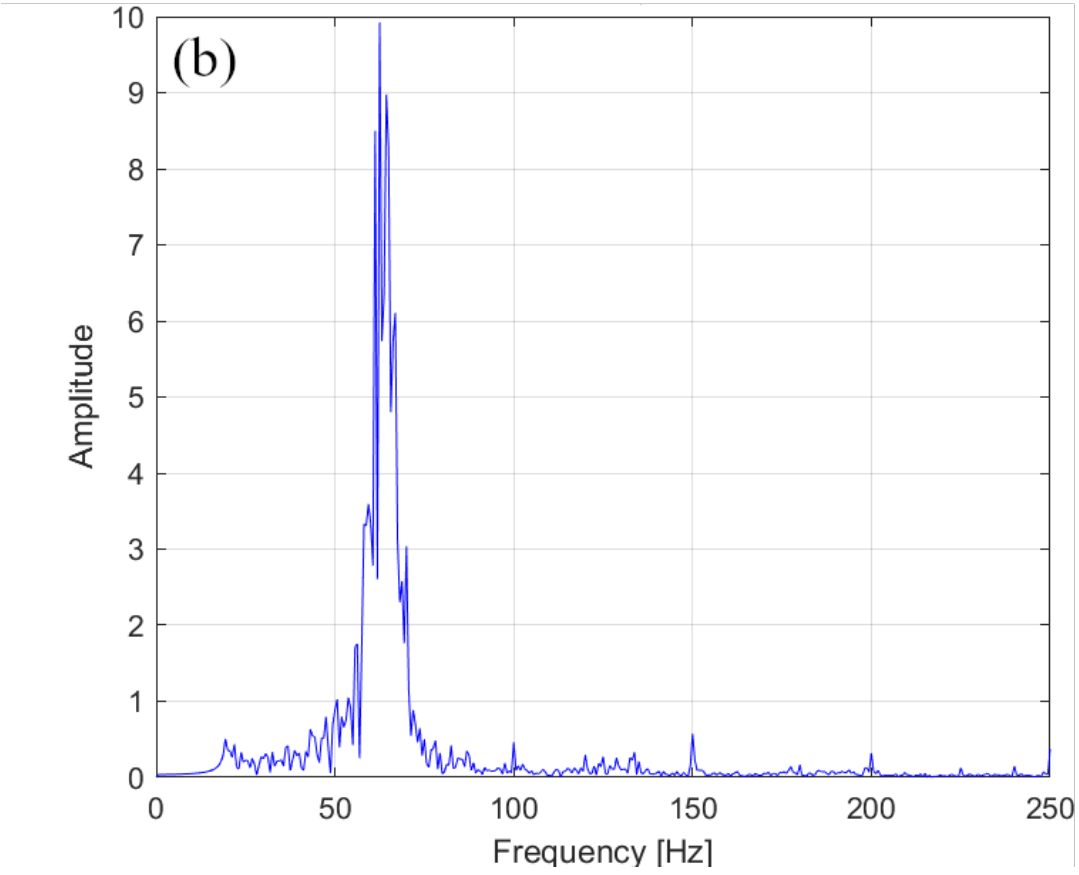

Fig. 6.16. (a) Pressure signal of the experiment with h = 2 mm and ϕ = 0.36 (10.5% vol. H_2). (b) Fourier spectrum of that signal.

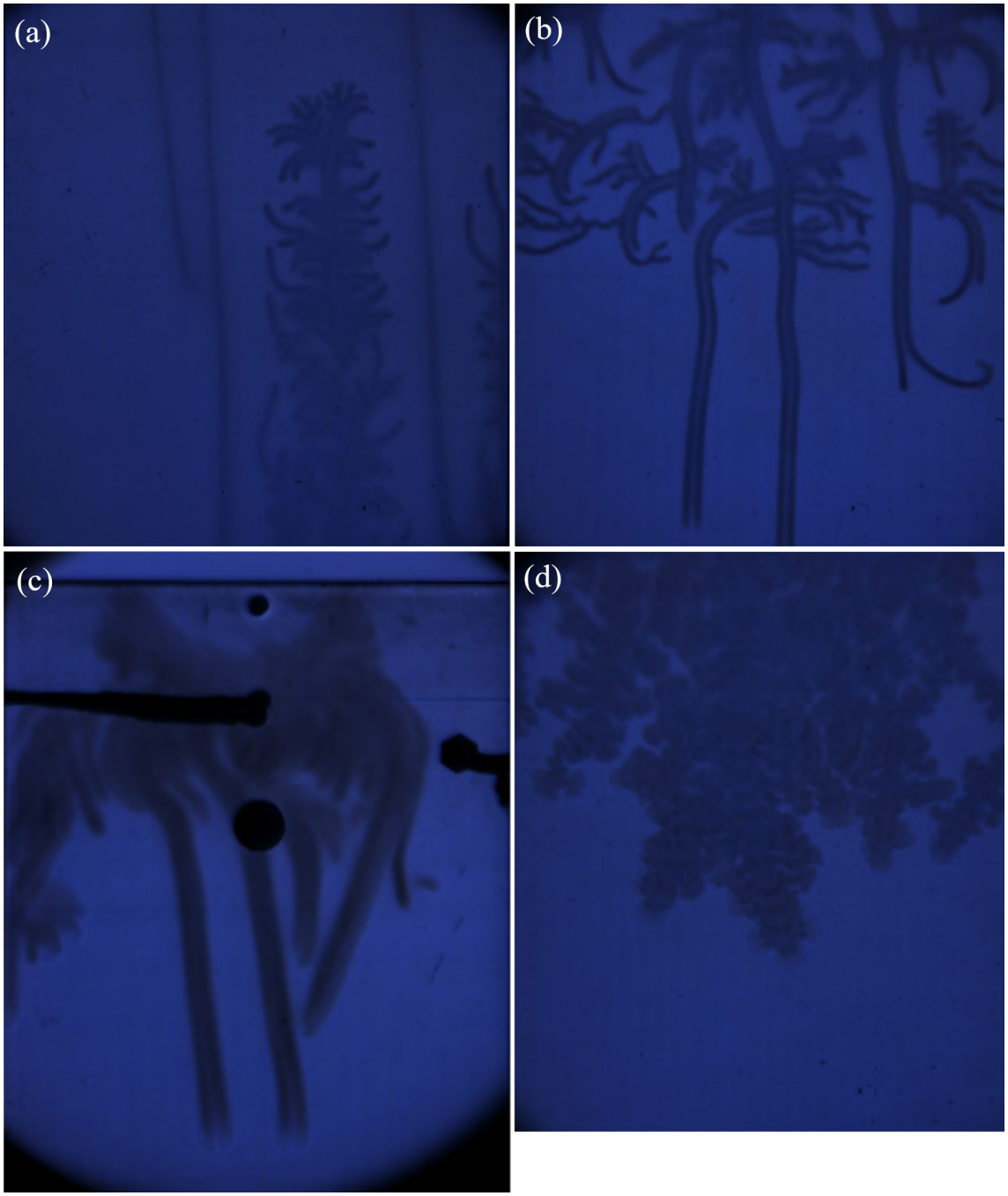

Fig. 6.17. Four samples of fractal instability images. (a) $h = 2$ mm and $\phi = 0.35$ (10.25% vol. H_2), upper part of the chamber. (b) $h = 2$ mm and $\phi = 0.36$ (10.5% vol. H_2), lower part of the chamber. (c) $h = 4$ mm and $\phi = 0.30$ (8.75% vol. H_2), ignition region. (d) $h = 1$ mm and $\phi = 0.49$ (14.5% vol. H_2), upper part of the chamber.

7. CONCLUSIONS

7.1. Objectives Achievement

Flame instabilities in thin channels are studied experimentally for hydrogen-air premixed laminar flames. In particular, the effect of mixture equivalence ratio and combustion chamber thickness on the transition between the different types of instabilities is assessed. To do so, an ImageJ macro is developed to post-process the images recorded during the experiment, and a Matlab script to obtain the data of interest (flame position, speed, and length).

These data, along with the pressure measurements and visual inspection of the videos, allow to identify the different flame instabilities. The results are summarized in a "stability map" (Fig. 6.1), which shows the dominating instability at a given equivalence ratio and chamber thickness conditions.

The existence of a primary thermoacoustic instability region is confirmed for mixtures leaner than those giving secondary instabilities, in chambers of thickness 4-8 mm. This fact is only reported by Veiga-López [1]. This is due increasing heat losses as equivalence ratio, and hence thermal flame thickness, decreases.

Also, a new kind of instability, which is not found in the literature, is identified. It occurs for very lean mixtures (just above the flammability limit) in a very thin chamber (chamber thickness up to 4 mm), and is characterized by tiny flame fronts that follow fractal-like paths, somewhat resembling tree branches or leaves. It is hypothesized that this fractal instability is due to large heat losses by conduction, when the chamber walls are close to each other.

An interesting feature of these fractal instabilities that the flame fronts are split in two symmetrical "heads", somewhat similar to the the symmetrical triangular patterns observed in the early combustion stages of slightly richer mixtures (e.g. see Fig. 6.12(a)).

7.2. Future Research

Here are some potential follow-ups of this project:

- Including variables such as the Markstein number and the average propagation speed in the characterization of the different instabilities.
- A study of the effect of combustion chamber walls deformation due to pressure oscillations, which might be non-negligible for secondary theromacoustic instabilities (~5 kPa max. over-pressure).

- A similar analysis of flames propagating upward, and/or from the closed end of the chamber toward the open one.
- A more detailed study of the fractal instability, including variables such as flame front width (i.e. “diameter” of the double heads), more accurate propagation speed, etc., and providing an explanation why the flame fronts are divided in two symmetrical halves (or heads).
- Optimization of the ImageJ macro and the Matlab script, to reduce computation time and automatize the adjustment of program variables depending on the particular experiment case. The possibility of implementing an artificial intelligence algorithm to more effectively detect the flame front on the images could be considered.

8. PROJECT MANAGEMENT

This chapter includes legal, economic, and organizational aspects of the project.

8.1. Socioeconomic Impact

This project has no direct real-life application, but is intended to better understand the mechanisms producing flame instabilities and to provide an experimental basis for mathematical models that would allow to predict flame instabilities in industrial applications. All instabilities described in this project are also observed in more realistic setups and conditions: complex-geometry combustion chambers, turbulent flows, etc. [2]

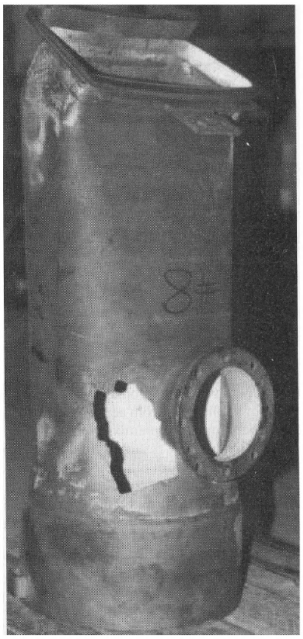

Fig. 8.1. A component of a power-plant combustor after destructive combustion instability has occurred. Courtesy of Di Vita [25].

Among the different kinds of instabilities, thermoacoustic ones are especially interesting, because they are generally undesirable. All systems using confined combustion, such as rocket engines, gas turbines, or furnaces, are prone to thermoacoustic instabilities, which might have detrimental consequences [2]. On top of that, in the case of power generating turbines and industrial furnaces, premixed lean combustion is the most common choice to reduce pollution. These conditions also increase the likelihood of thermoacoustic effects [25].

Thermoacoustics cause periodic loads, which cause material fatigue. This is a major concern in gas turbines and rocket engines design. The usual solution is to use an "artificial" control system, which adjusts combustor control parameters as soon as oscillations

are detected. In extreme cases, the engine or turbine may need to be shut down. Fig. 8.1 shows a part of a combustion chamber from a gas turbine for power generation damaged by combustion instability.

Another application (less direct, and more futuristic) this project may be useful for is the development of portable power generation systems. There is a variety of application areas, such as unmanned aerial vehicles, power sources for portable electronics, fast-deployment generators in remote areas or immediately after natural catastrophes, which do not require high power (usually they are in the 1-100 W range) but do require higher specific energy than batteries.

A solution proposed by engineers at the University of California in Berkeley, is pocket-sized Wankel rotary engine [8, 26, 27], shown in Fig. 8.2. The main drawback of such small internal combustion engines is their extremely performance. This is due to high surface-to-volume ratios that increase heat losses and short residence time that make complete combustion difficult. This project might help to better understand heat losses mechanisms in reduced-size combustion chambers.

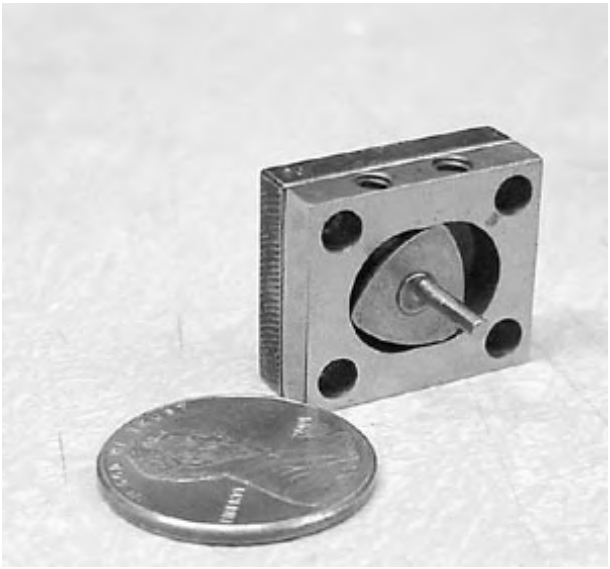

Fig. 8.2. Small rotary Wankel engine developed at the University of California in Berkeley, capable of producing up to 2.5 W of electricity. It runs on hydrocarbon fuels, and 30 ml of fuel keeps it running for two hours. At the time it was built, it was the smallest engine of its kind in the world. Courtesy of the University of California [27].

It is also important to remark that hydrogen is an emerging alternative fuel nowadays [28]. Currently it not frequently used, because of its low volumetric energy density and explosion hazard. However, it has many desirable characteristics, such as high mass-specific heating energy, clean emissions, and low-cost production. Additionally, it can be used both as conventional combustion fuel, and in hydrogen fuel cells.

As for the fractal instabilities, which appear for very lean mixtures in very thin channels, could possibly take place in hydrogen fuel cells. This is a subject of current research.

8.2. Regulatory Framework

Even though this project does not directly involve hydrogen combustion experiments, it is important to remark that hydrogen manipulation is extremely hazardous. Hydrogen has an ignition energy lower than that of most hydrocarbons, which makes unintended auto-ignition more likely.

In the experiment analyzed in this project, certified ultra-high purity grade hydrogen (99.999%) is used. It is stored as high-pressure gas in gas cylinders. The hydrogen storage and manipulation equipment at the facilities where the experiments were carried out, is AIAA G-095A-2017 compliant. The AIAA G-095A-2017 is an internationally accepted hydrogen systems safety standard guide. Fig. 8.3 show typical hazard placards posted on stationary hydrogen facilities.

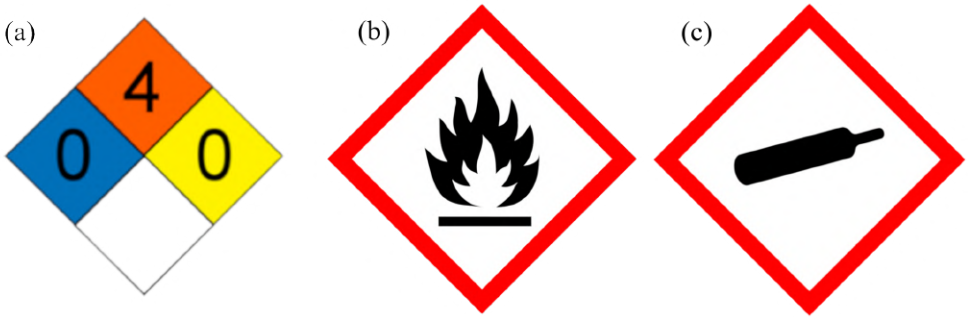

Fig. 8.3. Hazard placards posted on stationary hydrogen facilities, as recommended by the Government of Spain [29]. (a) NFPA 704 gaseous hydrogen fire diamond. It is an American fire protection standard, sometimes used in Europe. The number in the red field stands for the flammability level, the blue one for health hazards, the yellow one for stability level, and the white field is reserved for special notices. Courtesy of the U.S. Department of Energy [30]. (b) Fire hazard GHS (Globally Harmonized System) pictogram. (c) Compressed gas hazard GHS pictogram.

Another important aspect is the technical standards used in the development of the project. In this project, standard practices related to programming languages are applied. This is important to make programs easier to understand, modify and/or extend in the future. In particular, the Matlab scripts are written following *Matlab Style Guidelines* [31]. ImageJ macros have their own, Java-based programming language, named ImageJ Macro language (IJM). In this project the Google Java Style Guide [32] is followed.

8.3. Time Planning

In total, it takes 8 months, with an average dedication of 10 h a week, to carry out this project.

The phases of the project are the following:

- Preliminary planning: Objectives definition, initial time planning, etc.
- Bibliographic review: Bibliographic research to become familiar with the concepts of flame instabilities and digital image processing, determination of the state-of-the-art.
- ImageJ macro development
- Matlab programs development
- Data processing and analysis: Apply the macro and the programs to analyze the images and pressure measurements, and obtain relevant graphs and plots. Some additional bibliographic revew is required to compare the results with the literature.
- Paper writing: Reporting the results in a clear way
- Paper review by the advisor.

These phases are summarized in Fig. 8.4, along with approximate timing of each of them. Also, during the development of the project, the author has meetings with the advisor every two weeks approximately, to report progress made, as well as difficulties and problems.

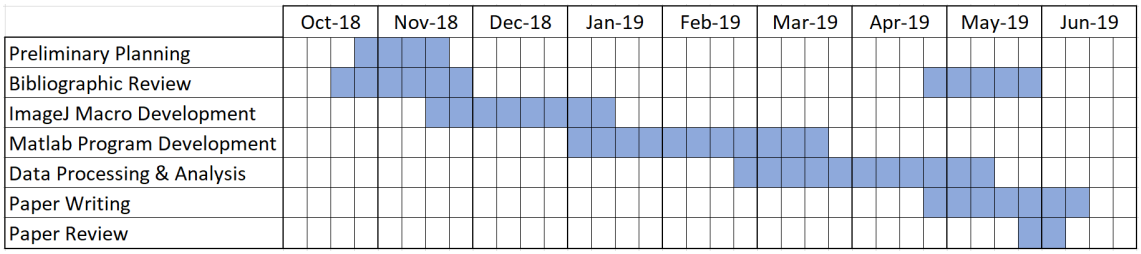

Fig. 8.4. Project time planning

8.4. Project Budget

In this section, the cost of the project is estimated. The cost of the experiment itself is not analyzed since it is out of scope of the project (this project is just about experimental data analysis).

The main expense related to this project is the salary of the person carrying it out. The usual wage of an undergraduate research assistant is about € 5 an hour. Time dedication is estimated to be 10 h a week on average, for eight months.

Low-cost academic license is available for Matlab. Additionally, a special Matlab image processing toolbox is used in this project. Other required software (Ubuntu operating system, ImageJ, Gimp, Inkscape) and online applications (Overleaf LaTeX document editor) are free. The only hardware tool is a desktop computer.

In the estimation of hardware and software resources cost, an approximated amortization period and actual project used time are included. Also, a 10% risk for unforeseeable expenses is considered.

Table 8.1. PROJECT BUDGET BREAKDOWN

Concept	**Quantity**	**Price**	**Amortization Period**	**Time used**	**Cost**
Personnel					
Undergraduate Student	320 h	€5/h	N/A	N/A	€1,600
Resources					
Desktop Computer	1	€700	36 months	8 months	€156
Matlab Student License	1	€35	24 months	8 months	€12
Matlab Image Processing Toolbox	1	€20	24 months	8 months	€7
Total					€1,775
Risk (10%)					€178
Grand Total					€1,953

The total cost of the project turns out to be €1,953.

BIBLIOGRAPHY

[1] F. Veiga-López, D. Martínez-Ruiz, M. Kuznetsov, and M. Sánchez-Sanz, "Thermoacoustic study of lean air-hydrogen premixed flames in narrow channels", in *11th Mediterranean Combustion Symposium*, Tenerife (Spain), Jun. 2019.

[2] P. Clavin and G. Searby, *Combustion Waves and Fronts in Flows: Flames, Shocks, Detonations, Ablation Fronts and Explosion of Stars*. Cambridge (UK): Cambridge University Press, 2016, pp. 55–105.

[3] M. Matalon, "Intrinsic flame instabilities in premixed and nonpremixed combustion", *Annu. Rev. Fluid Mech*, no. 39, pp. 163–191, 2007.

[4] D. Fernández-Galisteo, V. N. Kurdyumov, and P. D. Ronney, "Analysis of premixed flame propagation between two closely-spaced parallel plates", *Combustion and Flame*, vol. 190, pp. 133–145, 2018.

[5] B. Denet and P. Haldenwang, "Numerical study of thermal-diffusive instability of premixed flames", *Combustion Science and Technology*, no. 86, pp. 199–221, 1992.

[6] J. P. Hathout, "Thermoacoustic instability", in *Fundamentals and Modeling in Combustion. Volume 2.280*, Apr. 1999. [Online]. Available: `http://citeseerx.ist.psu.edu/viewdoc/summary?doi=10.1.1.40.1759`.

[7] F. Veiga-López, D. Martínez-Ruiz, E. Fernández-Tarrazo, and M. Sánchez Sanz, "Experimental analysis of oscillatory premixed flames in a Hele-Shaw cell propagating towards a closed end", *Combustion and Flame*, no. 201, pp. 1–11, Mar. 2019.

[8] J. Palacios-Mambrilla, *Análisis de imágenes mediante Matlab para experimentos de combustión*, Master Thesis, Universidad Carlos III de Madrid, 2018.

[9] J. Yanez, M. Kuznetsov, and J. Grune, "Flame instability of lean hydrogen-air mixtures in a smooth open-ended vertical channel", *Combustion and Flame*, no. 162, pp. 2830–2839, 2015.

[10] J. Tyndall, *Sound*. New York: P. F. Collier & Son, 1902. [Online]. Available: `http://www.gutenberg.org/ebooks/54969`.

[11] C. A. A. Atis, M. Sarker, and M. Ehsan, "Study of thermoacoustic phenomenon in a Rijke tube", *Procedia Engineering*, no. 90, pp. 569–574, 2014.

[12] J. W. S. Rayleigh, "The explanation of certain acoustical phenomena", *Nature*, no. 18, pp. 319–321, 1878.

[13] G. Searby, "Acoustic instability in premixed flames", *Combust. Sci. and Tech*, no. 81, pp. 221–231, 1992.

[14] J. D. Buckmaster and G. S. S. Ludford, *Theory of Laminar Flames*, eng, ser. Cambridge monographs on mechanics and applied mathematics. Cambridge: Cambridge University Press, 1982.

[15] S. H. Yoon, T. J. Noh, and O. Fujita, "Onset mechanism of primary acoustic instability in downward-propagating flames", *Combustion and Flame*, no. 170, pp. 1–11, 2016.

[16] R. C. Aldredge and N. Killingsworth, "Experimental evaluation of Markstein-number influence on thermoacoustic instability", *Combustion and Flame*, no. 137, pp. 178–197, 2004.

[17] E. Al-Sarraf, C. Almarcha, B. Radisson, J. Quinard, and B. Denet, "Premixed flame instability in a Hele-Shaw burner", in *XXIV ICTAM*, Montreal (Canada), Aug. 2016, pp. 21–26.

[18] C. Almarcha *et al.*, "Experimental two dimensional cellular flames", *Physics of Fluids*, no. 27:091110, 2015.

[19] A. Petchenko, V. Bychkov, V. Akkerman, and L.-E. Eriksson, "Violent folding of a flame front in a flame-acoustic resonance", *Physical Review Letters*, vol. 97, p. 164 501, 16 Oct. 2006.

[20] A. Petchenko, B. Bychkov, V. Akkerman, and L.-E. Eriksson, "Flame–sound interaction in tubes with nonslip walls", *Combustion and Flame*, vol. 149, no. 4, pp. 418–434, 2007.

[21] R. W. Schefer, W. D. Kulatilaka, B. D. Patterson, and T. B. Settersten, "Visible emission of hydrogen flames", *Combustion and Flame*, no. 156, pp. 1234–1241, 2009.

[22] T. Ferreira and W. Rasband, *ImageJ User Guide*, 2012. [Online]. Available: `https://imagej.nih.gov/ij/docs/guide/`.

[23] R. C. Gonzalez and R. E. Woods, *Digital Image Processing*, 4th ed. New York: Pearson, 2017.

[24] M. H. Trauth, *Data voids and spectral analysis: Don't be afraid of gaps!*, University of Potsdam, 2017. [Online]. Available: `http://mres.uni-potsdam.de/index.php/2017/08/22/data-voids-and-spectral-analysis-dont-be-afraid-of-gaps/`.

[25] A. Di-Vita, "On Rayleigh's criterion of thermo-acoustics", PhD thesis, Universitá di Genova, 2013.

[26] S. Bennet Sprague, S. W. Park, D. C. Walther, A. P. Pisano, and A. C. Fernandez-Pello, "Development and characterisation of small-scale rotary engines", *International Journal of Alternative Propulsion*, pp. 275–293, 2007.

[27] C. Zandonella, *Engineers create world's smallest rotary internal combustion engine*, University of California, 2001. [Online]. Available: `www.berkeley.edu/news/berkeleyan/2001/04/10_cmbus.html`.

[28] *Hydrogen basics*, U.S. Department of Energy. Enery Efficiency & Renewable Energy, 2018. [Online]. Available: https://afdc.energy.gov/fuels/hydrogen_basics.html.

[29] A. Perez-Guerrero, "Ntp 566: Señalización de recipientes y tuberías: Aplicaciones prácticas", Tech. Rep., 2000. [Online]. Available: https://www.insst.es/InshtWeb/Contenidos/Documentacion/FichasTecnicas/NTP/Ficheros/501a600/ntp_566.pdf.

[30] *Hydrogen safety tips for first responders*, U.S. Department of Energy. Hydrogen Program, 2017. [Online]. Available: www.dhses.ny.gov/ofpc/publications/documents/HydrogenPoster_v15.pdf.

[31] R. Johnson, *Matlab Style Guidelines 2.0*. Datatool, 2014. [Online]. Available: http://datatool.com/resources.html.

[32] Google, *Google Java Style Guide*, 2015. [Online]. Available: https://google.github.io/styleguide/javaguide.html#s4-formatting.

[33] J. Yanez, M. Kuznetsov, and R. Redlinger, "The acoustic-parametric instability for hydrogen-air mixtures", *Combustion and Flame*, no. 160, pp. 2009–2016, 2013.

[34] N. Peters and B. Rogg, *Reduced Kinetic Mechanisms for Applications in Combustion Systems*. Springer, 1993.